ESTIMATING REGIONAL MEAN CONDUCTIVITY PROFILES AND DETECTING GALVANIC DISTORTION USING MAGNETOTELLURIC ROTATIONAL INVARIANTS

TAWAT RUNG-ARUNWAN

A THESIS SUBMITTED IN PARTIAL FULFILMENT
OF THE REQUIREMENTS FOR
THE DEGREE OF DOCTOR OF PHILOSOPHY
(PHYSICS)
FACULTY OF GRADUATE STUDIES
MAHIDOL UNIVERSITY
2016

Thesis

entitled

ESTIMATING REGIONAL MEAN CONDUCTIVITY PROFILES AND DETECTING GALVANIC DISTORTION USING MAGNETOTELLURIC ROTATIONAL INVARIANTS

.....
Mr. Tawat Rung-Arunwan
Candidate

.....
Assoc. Prof. Weerachai Siripunvaraporn,
Ph.D. (Geophysics)
Major advisor

.....
Prof. Hisashi Utada,
D. Sc. (Geophysics)
Co-advisor

.....
Asst. Prof.Pichet Kittara,
Ph.D. (Physics)
Co-advisor

.....
Lect.Chaiwoot Boonyasiriwat,
Ph.D. (Scientific Computing)
Co-advisor

.....
Prof. Patcharee Lertrit,
M.D., Ph.D. (Biochemistry)
Dean
Faculty of Graduate Studies

.....
Assoc. Prof. Weerachai Siripunvaraporn,
Ph.D. (Geophysics)
Chair
Doctor of Philosophy Programme
in Physics
Faculty of Science

Thesis

entitled

ESTIMATING REGIONAL MEAN CONDUCTIVITY PROFILES AND DETECTING GALVANIC DISTORTION USING MAGNETOTELLURIC ROTATIONAL INVARIANTS

was submitted to the Faculty of Graduate Studies, Mahidol University
for the degree of Doctor of Philosophy (Physics)
on
February 24, 2016

.....
Mr. Tawat Rung-Arunwan
Candidate

.....
Dr. Siriporn Chaisri,
Ph.D. (Geophysics)
Chair

.....
Assoc. Prof. Weerachai Siripunvaraporn,
Ph.D. (Geophysics)
Member

.....
Lect. Chaiwoot Boonyasiriwat,
Ph.D. (Scientific Computing)
Member

.....
Prof. Hisashi Utada,
D. Sc. (Geophysics)
Member

.....
Prof. Patcharee Lertrit,
M.D., Ph.D. (Biochemistry)
Dean
Faculty of Graduate Studies
Mahidol University

.....
Assoc. Prof. Sittiwat Lertsiri,
Ph.D. (Agricultural Science)
Dean
Faculty of Science
Mahidol University

ACKNOWLEDGEMENTS

Sincerely, I profoundly thank Assoc. Prof. Weerachai Siripunvaraporn and Prof. Hisashi Utada for their advices, encouragement and patience throughout my study.

Also, I am very thankful to members of Geophysics Research Group, Mahidol University. Most importantly, I am very grateful to my family for their strong support.

This study was supported by the Researching Assistant scholarship by the Thailand Center of Excellence in Physics (ThEP) and the intership program by the Earthquake Research Institute, the University of Tokyo, Japan.

Most of figures were produced using the Generic Mapping Tools (GMT) software.

Tawat Rung-Arunwan

ESTIMATING REGIONAL MEAN CONDUCTIVITY PROFILES AND DETECTING GALVANIC DISTORTION USING MAGNETOTELLURIC ROTATIONAL INVARIANTS.

TAWAT RUNG-ARUNWAN 5338860 SCPY/D

Ph.D. (PHYSICS)

THESIS ADVISORS : WEERACHAI SIRIPUNVARAPORN, Ph.D. (GEOPHYSICS), HISASHI UTADA, D. Sc. (GEOPHYSICS), PICHET KITTARA, Ph.D. (PHYSICS), CHAIWOOT BOONYASIRIWAT, Ph.D. (SCIENTIFIC COMPUTING)

ABSTRACT

Having a reliable regional mean conductivity profile is useful and informative in interpreting magnetotelluric (MT) data. Traditionally, the Berdichevsky average, the average determinant (det; which is an rotational invariant property) impedance, is used to estimate the regional mean conductivity profile. Nonetheless, the det impedance is found to be biased downward by galvanic distortion. As a consequence, the Berdichevsky average may overestimate the regional mean conductivity profile. On the contrary, the sum-of-the-squared-elements (ssq) impedance is less sensitive to such an effect. Using the average ssq impedance is a sensible choice to estimate the regional mean conductivity profile. In addition, the combination of det and ssq impedances enables us to indicate the existence and strength of galvanic distortion in MT data. The local and regional distortion indicators are introduced to quantify the strength of the shear and splitting effects in galvanic distortion at individual stations and throughout the dataset, respectively. The apparent gains are defined and proven to be a good approximation of the site gain, which is generally claimed to the non-determinable distortion parameters. These findings are advantageous and able to solve several problems with MT datasets in performing 3D inversion.

KEY WORDS : MAGNETOTELLURICS / ROTATIONAL INVARIANT REGIONAL STUDIES / GALVANIC DISTORTION

78 pages

ยฐโีโยชโ๊โยกโ์โศ (ESTIMATING REGIONAL MEAN CONDUCTIVITY PROFILES AND DETECTING GALVANIC DISTORTION USING MAGNETOTELLURIC ROTATIONAL INVARIANTS).

โีโยซีโีข โ๊รฟร่รจรีโ๊รฟโ็ศยซโ๊โ็ศ 5338860 SCPY/D

ยชโ๊.ยศ. (โ•ยศยรีโซ)

ยงโ็ศโยฐโ๊โยกยฐโ๊โยงยซโซยงรฟยกยซโ่โ•ยณโ์ฯโร่ฆฯโ็รศ : ยซโ๊โ๊โีขโ็ยณ ยโ๊โ่รฆโ็ฯโ็รํยซโ๊โยฟโ๊โศํ, Ph.D. (GEOPHYSICS), โ๊ยถโร๊รฒโร๊ยฐโ๊ร•ยขโร๊ยถโ๊รรป ยณโ๊โร๊รฒยณร่โ๊รรจโร๊รบโ๊รรถโร๊รบ, D. Sc. (GEOPHYSICS), โ๊ร•ยขโร๊รฎยณยจยณยดโ๊รธโ๊รขยงโร๊รฒ โ๊รยดโ๊รธโ๊รขโ๊โรขโยณยชโร๊รฒโ๊รรถโร๊รฒยณยดโร๊รฎโ๊รขยงล็รี๊โ๊รจ, Ph.D. (PHYSICS), CHAIWOOT BOONYASIRIWAT, Ph.D. (SCIENTIFIC COMPUTING)

โซโ•ยงโ็โยศยณรรี

Thai abstract XXX

78 รฯรขโ์

CONTENTS

CONTENTS (cont.)

LIST OF FIGURES

LIST OF FIGURES (cont.)

LIST OF FIGURES (cont.)

CHAPTER I

INTRODUCTION

The Earth's physical properties can be either explicitly or implicitly derived from geophysical studies. Integrating several physical properties are beneficial for subsurface inverstigation. The electrical conductivity or *inverse* resistivity, which defines how materials allow or oppose current flow, is one of the most informative attributes because it can be related to a number of properties such as temperature, pressure, porosity, fluid content, and chemical compositions, for example. Thus, including the Earth's conductivity structure with other physical properties makes geological interpretation more reliable. For instance, the conjunction of Earth's conductivity structure and its seismic structure helps complement our understanding of the Earth's interior. The conductivity structure itself is not only related to thermal structure but also to the water content in the mantle's minerals (e.g., Karato, 1990; Yoshino et al., 2006; Wang et al., 2006), which is believed to play an important role in mantle dynamics and evolution (e.g., Kelbert et al., 2009; Baba et al., 2010; Shimizu et al., 2010). Also, studying the crustal structure in terms of its conductivity together with other physical properties helps us to better understand tectonic setting and its transformation (e.g., Muller et al., 2009; Unsworth, 2010; Boonchaisuk et al., 2013). Knowing the subsurface conductivity structure is also profitable for exploration purposes. For example, the geothermal settings are evidently characterized by its electrical conductivity signature (see a review paper by Muñoz, 2013, and references therein).

From the historical perspective, revealing the Earth's conductivity structure originates from analysing the Earth's magnetic field – the geomagnetic depth sounding (GDS) method (Chapman and Price, 1930; Banks, 1969; and also a review by Tarits, 1994). In these papers, the 1D conductivity profiles were obtained

from geomagnetic observation at a individual site, where the lateral heterogeneity in the Earth (including continents and oceans) were ignored. The GDS method is most senstive to the conductivity structure at upper- and mid-mantle depths, where the corresponding signals have a period of a day or more. The geomagnetic signals in this range are valid under the assumption that the source field variation is expressed as the external dipole. Later on, it is possible to construct the global 3D conductivity model by performing the global induction studies using global geomagnetic data (e.g., Fukao et al., 2004; Koyama et al., 2006; Kelbert et al., 2008; Kuvshinov, 2008; Utada et al., 2009). Recent progress in global induction studies can be found in Kuvshinov (2011).

In global-scale studies, we can write the conductivity distribution $\sigma(z, \theta, \phi)$ at an arbitrary position in the Earth as the combination of the global mean 1D conductivity profile $\sigma_0(z)$ and the azimuthal conductivity contrast $\Delta\sigma(z, \theta, \phi)$:

$$\sigma(z, \theta, \phi) = \sigma_0(z) + \Delta\sigma(z, \theta, \phi). \tag{1.1}$$

Also, we may define the global mean 1D conductivity profile as the azimuthal average conductivity from any conductivity distribution:

$$\sigma_0(z) = \frac{1}{S_0(z)} \oiint \sigma(z, \theta, \phi)\, \mathrm{d}S, \tag{1.2}$$

where $S_0(z)$ is the total surface area of the Earth at depth z and $\mathrm{d}S$ is an element of the Earth's surface. Also, we may use the logarithmic average,

$$\log \sigma_0(z) = \frac{1}{S_0(z)} \oiint \log \sigma(z, \theta, \phi)\, \mathrm{d}S. \tag{1.3}$$

Since the global mean 1D conductivity profile is defined as the azimuthal average, the variance of $\Delta\sigma(z, \theta, \phi)$ is minimized in either a linear or logarithmic scale. Hence, the global mean 1D conductivity profile $\sigma_0(z)$ may be called an optimal global mean 1D conductivity profile. Although the definitions of the global mean 1D conductivity profile $\sigma_0(z)$ and the azimuthal contrast $\Delta\sigma(z, \theta, \phi)$ seem straightforward in theory, estimating them may be difficult in practice. One approach to

yield the reliable global 3D conductivity structure $\sigma(z, \theta, \phi)$ is to start from using the appropriate global mean 1D conductivity profile $\sigma_0(z)$ as an initial or *a priori* model (e.g., Kelbert et al., 2008; Semenov and Kuvshinov, 2012). Nevertheless, the significant differences between existing inverted models (e.g., Kelbert et al., 2009; Kuvshinov and Semenov, 2012; Semenov and Kuvshinov, 2012) were still observed. These results may include biases due to the non-uniformity of their site distribution or spatial aliasing, because the distribution of geomagnetic observatories is generally non-uniform and sometimes very sparse especially in oceanic regions. Also, EM induction is sensitive to the underlying structure and may be affected by the heterogeneity nearby each observation site.

After the commencement of geomagnetic studies, the prospecting to use the geoelectric signals, i.e., the telluric current or electric fields, was investigated. The EM induction, the relation between the magnetic field and the induced telluric current, was independently studied by Rikitake (1946), Tikhonov (1950), and Cagniard (1953). The first two scientists focused on using the induction effect to study the electrical property of the Earth's crust, while Cagniard (1953) made it practical for exploration purposes and it is known as magnetotellurics or MT. MT is mostly used for the case where the induction scale length is much smaller than the radius of Earth so that the sphericity of Earth can be ignored, i.e., Earth is assumed flat. Such a case is called the local or regional induction study. In general, the regional-scale studies deal with a limited region of interest where a number of observations are made either on land or in a marine environment. With progressive developments particularly in MT data processing (e.g., Egbert, 1997; Chave and Thomson, 2004; Smirnov and Egbert, 2012) and inversion (e.g., Sasaki, 2001; Siripunvaraporn et al., 2005; Uchida and Sasaki, 2006; Avdeev and Avdeeva, 2009; Kelbert et al., 2014) in recent decades, imaging regional 3D conductivity distributions has become practical and has been applied in various applications ranging from very near-surface to mantle studies.

As with the global-scale study, the regional 3D conductivity distribution $\sigma(x, y, z)$ can be expressed as the combination of the regional mean 1D conductivity

profile $\sigma_{\mathrm{R}}(z)$ and the lateral conductivity contrast $\Delta\sigma(x, y, z)$:

$$\sigma(x, y, z) = \sigma_{\mathrm{R}}(z) + \Delta\sigma(x, y, z). \tag{1.4}$$

We can also define the regional mean 1D conductivity profile as the areal average of the conductivity distribution:

$$\sigma_{\mathrm{R}}(z) = \frac{1}{A_0} \oiint \sigma(x, y, z)\, \mathrm{d}A, \tag{1.5}$$

where A_0 is the area where the observations are distributed, and $\mathrm{d}A$ is a surface element. Alternatively, we may use the logarithmic average to define the regional mean 1D conductivity profile:

$$\log \sigma_{\mathrm{R}}(z) = \frac{1}{A_0} \oiint \log \sigma(x, y, z)\, \mathrm{d}A. \tag{1.6}$$

As with Eqs. (1.2) and (1.3), defining the regional mean 1D conductivity profile with the areal average would minize the variance of $\Delta(x, y, z)$ (either in a linear or logarithmic scale). Also, the regional mean 1D conductivity profile $\sigma_{\mathrm{R}}(z)$ is called a regionally optimized mean 1D conductivity profile. Note that the arithmetic average of the conductivity in a logarithmic scale is equivalent to the geometric average of conductivity in a linear scale. Mathematically, the logarithmic-scale average of the conductivity will give the more resistive structure compared to the linear average definition. We may invert the MT dataset to yield the 3D conductivity distribution directly. Alternatively, we may begin from estimating the reasonable model of the regional mean conductivity profile, and use it as an initial or *a priori* in inverting the data for the conductivity model $\sigma(x, y, z)$ or the conductivity contrast $\Delta\sigma(x, y, z)$ later.

Traditionally, the Berdichevsky average (Berdichevsky et al., 1980), which averages the rotational invariant determinant (det) impedances from a number of MT observations within an area of interest, is used to estimate the model of the regional mean 1D conductivity profile. Although the choice of initial or prior models, e.g., using either the homogeneous Earth or the profile estimated from the

Berdichevsky average, in 3D problems remains a matter of debate, the benefits of using the regional mean 1D model have been reported. Solving forward problem would become more reliable becaused of the optimized conductivtiy contrast, which results in a better-conditioned system of equations in forward modeling (Avdeev, 2005). Tada et al. (2014) configured the reasonable initial and prior models for 3D inversion from the regional mean 1D models estimated by using the Berdichevsky average (Baba et al., 2010). Avdeeva et al. (2015) also claimed that defining the starting model using the Berdichevsky average is better than using a homogeneous halfspace.

Although using MT to image 3D conductivity structure is feasible, MT suffers from the problem of galvanic distortion. Excellent review and tutorial papers on galvanic distortion are given by Jiracek 1990, Groom and Bahr 1992, and Ledo 2005. Galvanic distortion is the spatial aliasing in MT data due to near-surface small-scale heterogeneity, and it is unavoidable, particularly in the case of land MT observations. Inverting the galvanically distorted data without proper treatments or removal may lead to inaccurate or erroneous inverted models (Avdeeva et al., 2015; Tietze et al., 2015) due to the interference from artifacts caused by galvanic distortion.

In contrast to the marine cases (e.g., Baba et al., 2010), the classic example for the effect of galvanic distortion on regional MT studies on land is the work of Berdichevsky et al. (1980). Within the same area of observation, the effective apparent resistivity curves were shifted irregularly, but not deformed. They suspected that the local effect from galvanic distortion caused such an effect, and they also proposed the averaging approach to smooth out the local effect of galvanic distortion. However, their work was introduced to the EM community before the knowledge of galvanic distortion was well established. Thus, examining the reliability of the method to estimate the model of the regional mean 1D conductivity profile with the present knowledge of galvanic distortion is also interesting.

Since the problem of galvanic distortion was recognized, several works have been developed to deal with this problem. They are described in the following. Groom and Bailey (1989) and Bahr (1988) first proposed a parametric model for

galvanic distortion but in the framework of a regionally 2D structure. The Groom–Bailey model of galvanic distortion (Groom and Bailey, 1989) has been adopted in many galvanic distortion studies. For example, McNeice and Jones (2001) also proposed the tensor decomposition based on the Groom–Bailey model under the 2D Earth assumption. Gómez-Treviño et al. (2014) uses the rotational invariant impedances to solve the galvanic distortion, and their work is also scoped to the assumption of 2D regional structure only. Most of the work has to be limited to the assumption of 2D Earth, because solving the galvanic distortion in the 3D Earth the problem itself becomes underdetermined.

3D inversion based on the phase tensor (Caldwell et al., 2004) has been developed and it is shown to reliably recover the structure of interest (Patro et al., 2013; Tietze et al., 2015). However, the phase tensor-based inversion strongly depends on the initial models because the phase tensor itself is absent in magnitude. By introducing the additional constraint in the inversion, the 3D inversion with galvanic distortion has been also developed (e.g., Sasaki and Meju, 2006; Avdeeva et al., 2015). It is a promising approach to deal with the galvanic distortion problem.

In spite of the fact that the galvanic distortion has an effect on MT data, the method to identify the existence of galvanic distortion or quantify its strength in MT data has never been proposed. Although the inconsistency between the lateral gradient of the MT impedance and the vertical magnetic transfer function can suggest the presence of galvanic distortion (see Utada and Munekane, 2000), the usage of the inconsistency check may be difficult for practical purposes and it is never stated explicitly in their paper.

This thesis aims to solve two problems relating to galvanic distortion: first, proposing the method to reliably estimate the model of the regional mean 1D conductivity profile with the presence of galvanic distortion, and, second, indicating the existence and strength of galvanic distortion in MT data. As mentioned, using the optimal regional mean 1D conductivity profile as an initial or *a priori* model is a good start in performing 3D inversion. As a consequence, being capable of estimating the unbiased model of the regional mean 1D conductivity profile from

the set of distorted MT data is significant. Also, being able to quantify the strength of galvanic distortion in MT data is important, as we can determine the necessity of the treatment for galvanic distortion or the omission of the heavily distorted data. Thus estimating the reliable model of regional mean 1D conductivity profile and indicating the existence of galvanic distortion would be useful and informative and would help relieve several difficulties in 3D inversion.

CHAPTER II
THEORETICAL BACKGROUND

In this chapter, the theoretical background used in this work is given. We start with magnetotellurics and focus on the MT impedance tensor, and its rotational invariant attributes. Then we describe the Berdichevsky average which is used to estimate the regional structure. Lastly, the principle and mathematical formulation of galvanic distortion are provided.

2.1 Magnetotellurics

Electromagnetic induction is the interrelation between magnetic and electric fields within the Earth. By analogy with Faraday's law of induction, the time-varying Earth's magnetic field causes the electric field (or known as the telluric current), to flow within Earth, which acts like a conductor. The induction effect was independently observed by Rikitake (1946) and Tikhonov (1950), and it was used to investigate the electrical property of the Earth's crust. The induction effect was made practical for exploration purposes by Cagniard (1953) and is also known as magnetotellurics or MT.

On the Earth's surface, MT can image the Earth resistivity structure using the naturally-occurring magnetic and electric fields, which are governed by Maxwell's equations. Since it was introduced, MT data acquisition processing and interpretation have been continuously developed, and MT has been used in various applications: mantle studies (e.g., Berdichevsky et al., 1980; Baba et al., 2010); crustal studies (e.g., Heise et al., 2007; Unsworth, 2010; Boonchaisuk et al., 2013); ore exploration (e.g. Tuncer et al., 2006; Türkoğlu et al., 2009); geothermal exploration (e.g., Pellerin et al., 1996; Heise et al., 2008; Amatyakul et al., 2015); environmental applications (e.g., Unsworth et al., 2007); and many others.

MT impedance

The MT response or known as MT impedance is obtained from the linear relationship between the horizontal magnetic field $\mathbf{B}_\mathrm{h}$ to the horizontal electric field $\mathbf{E}_\mathrm{h}$ in the frequency domain. Given that the electric and magnetic fields are collected at the location $\mathbf{r}_i$, the MT impedance is written as

$$\begin{aligned} \mathbf{E}_\mathrm{h}(\mathbf{r}_i;\omega) &= \mathbf{Z}(\mathbf{r}_i;\omega)\,\mathbf{B}_\mathrm{h}(\mathbf{r}_i;\omega) \\ \begin{bmatrix} E_x(\mathbf{r}_i;\omega) \\ E_y(\mathbf{r}_i;\omega) \end{bmatrix} &= \begin{bmatrix} Z_{xx}(\mathbf{r}_i;\omega) & Z_{xy}(\mathbf{r}_i;\omega) \\ Z_{yx}(\mathbf{r}_i;\omega) & Z_{yy}(\mathbf{r}_i;\omega) \end{bmatrix} \begin{bmatrix} B_x(\mathbf{r}_i;\omega) \\ B_y(\mathbf{r}_i;\omega) \end{bmatrix}, \end{aligned} \tag{2.1}$$

where ω is the angular frequency, $\omega = 2\pi f$. The spatial and frequency dependence of the MT impedance will be omitted in the rest of this thesis. The transfer function $\mathbf{Z}$ (also called the impedance tensor) is a second rank 2×2 tensor with components Z_{xx} Z_{xy} Z_{yx} and Z_{yy}, or known as MT impedances, are complex-valued numbers. Here, the frequency dependent part was omitted. The subscripts x and y denote the orthogonal components of magnetic fields and electric fields pointing northward and eastward, respectively. The components are generally represented by the magnitude (apparent resistivity) and phase,

$$\begin{aligned} \rho_{a,ij} &= \frac{\mu_0}{\omega}|Z_{ij}|^2, \\ \phi_{ij} &= \arg(Z_{ij}). \end{aligned} \tag{2.2}$$

The MT impedance itself is able to indicate the Earth dimensionality. In the 1D Earth, the electric field (and also the magnetic field) are the same in any directions, and the electric and magnetic fields are related only in orthogonal directions. The MT impedance becomes antisymmetric with zero diagonal components:

$$\begin{aligned} Z_{xx} &= Z_{yy} = 0, \\ Z_{xy} &= -Z_{yx} = Z_{1\mathrm{D}}, \end{aligned} \tag{2.3}$$

where Z_{1D} denotes the impedance derived from the 1D structure. In the 2D situation, given that the observation coordinate is in the strike direction, the orthogonal components of the electric field and those of the magnetic field are different, but there is still no coupling between the same components of electric and magnetic fields. The off-diagonal components of MT impedance are no longer equivalent:

$$Z_{xy} \neq -Z_{yx}. \tag{2.4}$$

But, in general cases (3D situation), the elements of the impedance tensors become:

$$\begin{aligned} Z_{xx} &\neq 0, \\ Z_{yy} &\neq 0, \\ Z_{xy} &\neq -Z_{yx}. \end{aligned} \tag{2.5}$$

Rotational invariant

Theoretically, the impedance tensor could be defined without reference to any horizontal coordinate system, but in practice the impedance tensor must be specified to the coordinate of observation. Given that $\mathbf{Z}_{\mathrm{R}}$ is the impedance tensor in the regional or principal coordinate, which is generally defined as the strike coordinate in 2D studies but it has no definition in 3D situations, the representation of this impedance tensor specific to the coordinate of observation $\mathbf{Z}_{\mathrm{obs}}$, which is rotated by the angle θ relative to the principal coordinate in the clockwise direction, could be written as

$$\mathbf{Z}_{\mathrm{obs}} = \mathbf{\Theta}(\theta)\mathbf{Z}_{\mathrm{R}}\mathbf{\Theta}^{\mathrm{T}}(\theta), \tag{2.6}$$

where the rotational matrix is

$$\mathbf{\Theta}(\theta) = \begin{bmatrix} \cos\theta & \sin\theta \\ -\sin\theta & \cos\theta \end{bmatrix}. \tag{2.7}$$

The principal or regional impedance is dependent on the observation coordinate. An attribute of the impedance tensor that remains unchanged under the rotation of the observation coordinate is referred to as being rotationally invariant. For example the determinant of the impedance tensor:

$$\det(\mathbf{Z}_{\rm obs}) = \det(\mathbf{\Theta}\,\mathbf{Z}_{\rm R}\mathbf{\Theta}^{\rm T}) = \det(\mathbf{\Theta})\det(\mathbf{Z}_{\rm R})\det(\mathbf{\Theta}^{\rm T}) = \det(\mathbf{Z}_{\rm R}),$$

where the function of angle θ was omitted.

Since the beginning of MT, many rotational invariant properties of MT impedance have been introduced. For example, the determinant was used to estimate the regional structure (e.g., Berdichevsky et al., 1980). Swift's skew (Swift, 1967) and Bahr's skew (Bahr, 1988), which serve as the dimensionality indicators, was developed based on the rotationally invariant properties. However, after the systematic and thorough investigation by Szarka and Menvielle (1997), the set of rotational invariants was introduced and it is able to represent the impedance tensor. Weaver et al. (2000) introduced another selection of rotational invariants, which are able to constrain the subsurface structure geometry, and also a compact geometrical visualization of the impedance tensor using Mohr's circle.

Among the number of rotational invariants, we are interested in two of them. First, the determinant (det),

$$\det(\mathbf{Z}) = Z_{xx}Z_{yy} - Z_{xy}Z_{yx}, \tag{2.8}$$

and, second, the sum of the squared elements (ssq)

$$\mathrm{ssq}(\mathbf{Z}) = \mathrm{tr}(\mathbf{Z}^{\rm T}\mathbf{Z}) = Z_{xx}^2 + Z_{xy}^2 + Z_{yx}^2 + Z_{yy}^2, \tag{2.9}$$

where tr denotes the matrix trace. The corresponding det and the ssq impedances are defined as follows:

$$Z_{\rm det} = \sqrt{\det(\mathbf{Z})}, \tag{2.10}$$

and

$$Z_{\text{ssq}} = \sqrt{\text{ssq}(\mathbf{Z})/2}. \tag{2.11}$$

The coefficient of $1/\sqrt{2}$ was introduced in the definition of ssq impedance to conserve the impedance magnitude.

In MT, the determinant is a widely-used rotational invariant. It was applied in various applications, for example, in marine studies (e.g., Seama et al., 2007; Baba et al., 2010; Yang et al., 2010). Oldenburg and Ellis (1993) and Pedersen and Engels (2005) developed 2D MT inversion using the det impedance. Arango et al. (2009) used the det impedance to deal with 3D MT data. Tournerie and Chouteau (2002) and Avdeeva et al. (2015) used the average det impedances to construct the *a priori* model. Lezaeta and Haak (2003) introduced the current channeling indicator using the det impedance.

In contrast to the det impedance, the ssq impedance is less familiar to the induction community. It was first introduced by Szarka and Menvielle (1997) to form the complete set of MT rotational invariants and only a few applications were reported (e.g., Szarka et al., 2000, 2005). Romo et al. (2005) used the det and ssq equivalents to define another representation of MT impedance. Gómez-Treviño et al. (2014) proposed the method to solve galvanic distortion in a 2-D regional structure with the det and ssq impedances.

2.2 Estimating the model of regional mean conductivity profile: The Berdichevsky average

Berdichevsky et al. (1980) conducted the regional-scale study of the conductivity structure of the Baikal region. The effective resistivity sounding curves, which are equivalent to the apparent resistivity derived from the det impedance (Eq. 2.10), within any regions were observed to be shifted, but not deformed (Figure 2.1). The shift in the effective resistivity was a manifestation of local galvanic distortion, and its distribution was shown to be log-normally distributed. In his

work, the effect of galvanic distortion at the ith observation was modeled as:

$$\rho^i_{\text{eff}} = K^i \rho_{\text{N}}, \tag{2.12}$$

where K^i is a random distortion coefficient following the log-normal distribution, ρ_{N} represents the regional impedance, ρ^i_{eff} is the observed effective impedance.

Through the cluster of m observations, the regional impedance was obtained from averaging the observed effective resistivities so as to smooth out the local effect due to galvanic distortion:

$$\bar{\rho}_{\text{eff}} = \left[\prod_{i=1}^{m} \rho^i_{\text{eff}}\right]^{\frac{1}{m}} = \left[\prod_{i=1}^{m} K^i\right]^{\frac{1}{m}} \rho_{\text{N}} \approx \rho_{\text{N}}. \tag{2.13}$$

The idea of averaging the impedances is regarded as one of the most practical solutions in regional studies (e.g., Baba et al., 2010) and also used to estimate an initial or *a priori* model in inversions (e.g., Tournerie and Chouteau, 2002; Tada et al., 2014; Avdeeva et al., 2015). However, the knowledge of galvanic distortion was not well-established at that time. Hence no detailed description of K^i was given.

In the following section, we re-examine the distorted effective impedance with the Groom–Bailey model of galvanic distortion (Groom and Bailey, 1989) and also his average approach in estimating the regional structure.

2.3 Galvanic distortion

Galvanic distorion is the alteration of electric field due to near-surface small-scale heterogeneity. In theory, the distortion of the MT data may be both galvanic and inductive, but we can choose a proper period range so that only the galvanic distortion is considered (Groom and Bahr, 1992; Utada and Munekane, 2000). In contrast to marine cases, most of on-land MT observations suffer from galvanic distortion. This section provides the physical principle of galvanic distortion, its mathematical formulation, and the galvanic distortion model or parame-

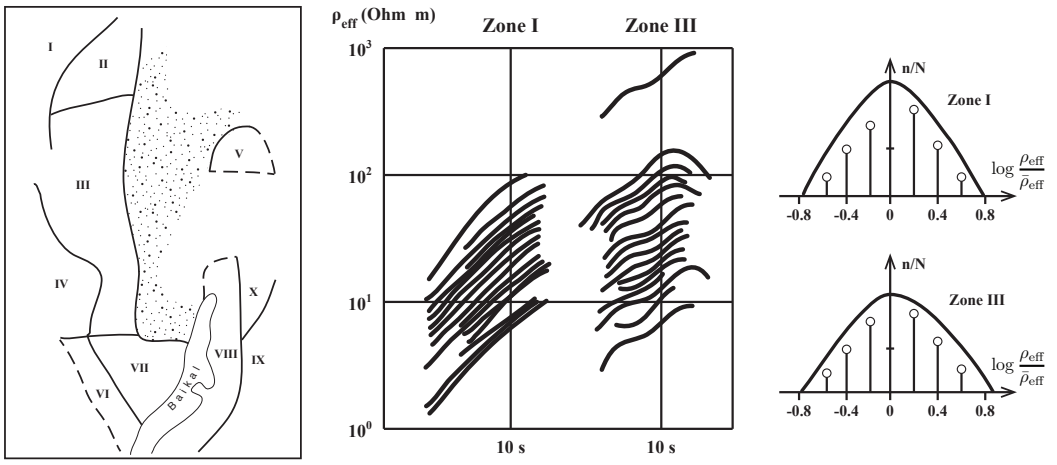

Figure 2.1: (left) Map of Baikal region divided into regions (denoted by numbers), where each has the same conformal effective resistivity curves. (middle) The effective resistivity curves and (right) the distribution of the coefficient K^i from data within Zone I and III (after Berdichevsky et al., 1980).

terization used in this work.

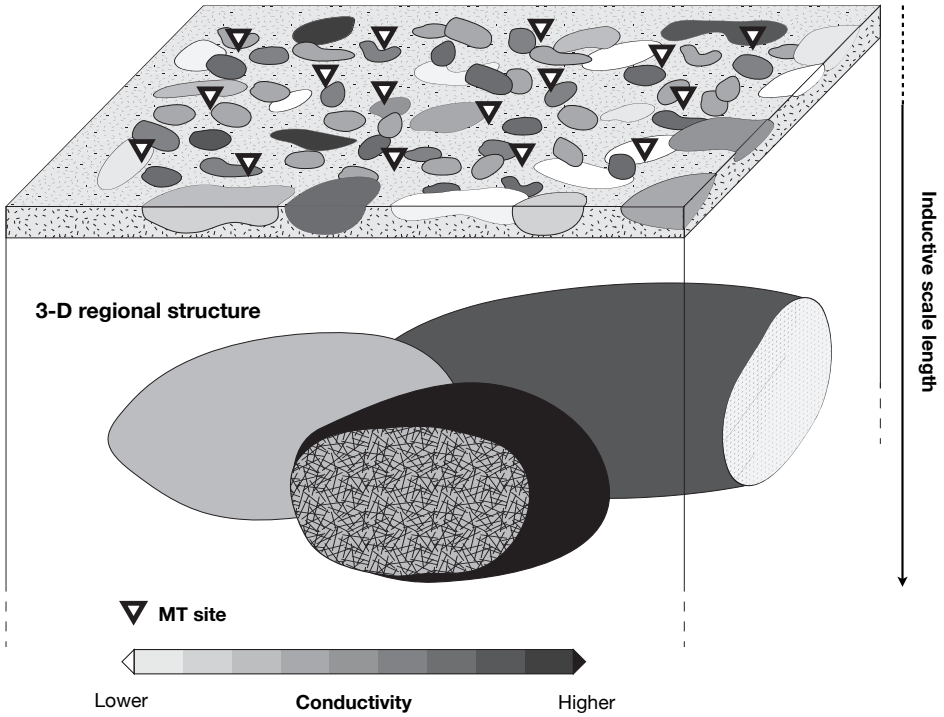

Figure 2.2: A model of galvanic distortion in this study. The model consists of 3D regional scale structure, which is of interest, and small-scale heterogeneities confined in the near-surface layer, which is shallower and thinner than the inductive scale length of interest (after Utada and Munekane, 2000; Rung-Arunwan et al., 2016).

2.3.1 Galvanic distortion principle

Following the formulation presented in Groom and Bahr (1992); Chave and Smith (1994) and Utada and Munekane (2000), this section provides the galvanic distortion principle based on electromagnetic scattering theory, which will leads to the mathematical representation of galvanic distortion.

According to Hohmann (1975), the electric field observed at an arbitrary position $\mathbf{r}$, both internal and external to the scatterer, from a 3D heterogeneous medium can be expressed as

$$\begin{aligned}\mathbf{E}(\mathbf{r}) = \mathbf{E}_{\mathrm{R}}(\mathbf{r}) - i\omega\mu_0 \sum_j \int_{V_j} g(\mathbf{r},\mathbf{r}')\,\delta\sigma_j(\mathbf{r}')\,\mathbf{E}(\mathbf{r}')\,\mathrm{d}V' \\ + \nabla\frac{1}{\sigma_0}\nabla\cdot\sum_j \int_{V_j} g(\mathbf{r},\mathbf{r}')\,\delta\sigma_j(\mathbf{r}')\,\mathbf{E}(\mathbf{r}')\,\mathrm{d}V',\end{aligned} \tag{2.14}$$

where V_j refers to each scattering body. Note that the quantities in Eq. (2.14) except the conductivity σ_0 and $\delta\sigma_j$ and the magnetic permeability μ_0 are frequency dependent, but they are implicitly written. The anomaly conductivity contrast $\delta\sigma_j(\mathbf{r}')$ is defined by

$$\delta\sigma_j(\mathbf{r}') = \sigma_j(\mathbf{r}') - \sigma_0(\mathbf{r}'), \tag{2.15}$$

where σ_j is the scatterer conductivity and σ_0 is the background or regional conductivity structure. The analytical expression of the Green's function of the uniform Earth is given by

$$g(\mathbf{r},\mathbf{r}') = \frac{e^{i\gamma_0|\mathbf{r}-\mathbf{r}'|}}{4\pi|\mathbf{r}-\mathbf{r}'|}, \tag{2.16}$$

where $\gamma_0 = \sqrt{i\omega\mu_0\sigma_0}$. The inductive scale length, or the electromagnetic skin depth, of the uniform background is

$$\lambda_0 = \frac{1}{|\Re\,\gamma_0|}. \tag{2.17}$$

From the expression of the electric field (2.14), the first term $\mathbf{E}_{\mathrm{R}}(\mathbf{r})$ is the field from the background structure, and the second and third terms denote the inductive and galvanic field components from each heterogeneity, which depends on size,

conductivity contrast and *inverse* distance. But only the inductive term contains the frequency dependent part, which vanishes at long periods.

The integral solution for the magnetic field could then be obtained by applying Faraday's law to Eq. (2.14);

$$\mathbf{B}(\mathbf{r}) = \mathbf{B}_{\mathrm{R}}(\mathbf{r}) + \mu_0 \nabla \times \sum_j \int_{V_j} g(\mathbf{r}, \mathbf{r}')\, \delta\sigma_j(\mathbf{r}')\, \mathbf{E}(\mathbf{r}')\, \mathrm{d}V', \tag{2.18}$$

In contrast to the electric field, the magnetic field (2.18) contains only the inductive term due to the heterogeneity. The galvanic component vanishes because of the vector calculus identity that the curl of gradient of any scalar function is the zero vector. Therefore, the galvanic effect comes from the electric field only.

The contribution from each scattering body or distorter could be determined by the induction number M_j,

$$M_j = \frac{L_j}{\lambda_j}. \tag{2.19}$$

which is the ratio of its horizontal dimension L_j to its inductive scale length

$$\lambda_j = 1/|\Re\, \gamma_j|, \tag{2.20}$$

where $\gamma_j = \sqrt{i\omega\mu_0\delta\sigma_j}$. The distorters are generally small in size and then have very small induction numbers. If these distorters are confined to the near-surface layer, shallower and thinner than the background inductive scale length (Figure 2.2), they produce the *visible* galvanic effect.

Ideally, if we have an infinitely dense MT survey and infinite band of data, all features could be explained by observation (Utada and Munekane, 2000). However, MT data is spatially insufficient because an MT array consisting of a limited number of sites is generally designed at least to cover the target structure with the typical site spacing that is able to resolve the smallest-scale target of interest. Therefore, the typical site spacing may be larger than the size of the distorters. The galvanic distorters inevitably cause spatial aliasing in MT data,

i.e., both interesting and irrelevant structures are included in the observation. Such an effect is called galvanic distortion. As it is impossible to recover original spatial features by using aliased data, the galvanic distorters are regarded as *unresolvable* structure (Booker, 2014). In order to obtain the reliable results, some treatments or augmented approaches to handle the galvanic distortion are essential.

The electric field solution in Eq. (2.14) could be simplified as

$$\mathbf{E}(\mathbf{r}) = \mathbf{E}_{\mathrm{R}}(\mathbf{r}) + \mathbf{e}_{\mathrm{I}}(\mathbf{r}) + \mathbf{e}_{\mathrm{G}}(\mathbf{r}), \tag{2.21}$$

where $\mathbf{e}_{\mathrm{I}}(\mathbf{r})$ and $\mathbf{e}_{\mathrm{G}}(\mathbf{r})$ represent the inductive and galvanic contributions from the scatterer. In the galvanic limit, Eq. (2.21) becomes

$$\mathbf{E}(\mathbf{r}) \approx \mathbf{E}_{\mathrm{R}}(\mathbf{r}) + \mathbf{e}_{\mathrm{G}}(\mathbf{r}) \tag{2.22}$$

When the size of each scatterer is sufficiently small, the background electric field can be regarded as uniform inside the scatterer. The horizontal vector of the galvanic field $\mathbf{e}_{\mathrm{G,h}}(\mathbf{r})$ can be related to the undistorted horizontal background electric field $\mathbf{E}^{\mathrm{h}}_{\mathrm{R}}(\mathbf{r})$ as

$$\mathbf{e}_{\mathrm{G,h}}(\mathbf{r}) = \alpha \mathbf{E}_{\mathrm{R,h}}(\mathbf{r}), \tag{2.23}$$

where α is a rank-2 real-valued tensor (see Chave and Smith, 1994). The observed *distorted* electric field (Eq. 2.22) then becomes

$$\mathbf{E}_{\mathrm{h}}(\mathbf{r}) = (\mathbf{I} + \alpha)\mathbf{E}_{\mathrm{R,h}}(\mathbf{r}) = \mathbf{C}\,\mathbf{E}_{\mathrm{R,h}}(\mathbf{r}), \tag{2.24}$$

where $\mathbf{C}$ is called the distortion operator, which is rank-2 real-valued tensor.

Within the scope of galvanic distortion, the distorted impedance tensor is expressed as the product between the distortion operator $\mathbf{C}$ and the regional

(undistorted) impedance tensor $\mathbf{Z}_{\mathrm{R}}$:

$$\begin{aligned}
\mathbf{Z}' &= \mathbf{C}\mathbf{Z}_{\mathrm{R}}, \\
\begin{bmatrix} Z'_{xx} & Z'_{xy} \\ Z'_{yx} & Z'_{yy} \end{bmatrix} &= \begin{bmatrix} C_{xx} & C_{xy} \\ C_{yx} & C_{yy} \end{bmatrix} \begin{bmatrix} Z^{\mathrm{R}}_{xx} & Z^{\mathrm{R}}_{xy} \\ Z^{\mathrm{R}}_{yx} & Z^{\mathrm{R}}_{yy} \end{bmatrix} \\
&= \begin{bmatrix} C_{xx}Z^{\mathrm{R}}_{xx} + C_{xy}Z^{\mathrm{R}}_{yx} & C_{xx}Z^{\mathrm{R}}_{xy} + C_{xy}Z^{\mathrm{R}}_{yy} \\ C_{yx}Z^{\mathrm{R}}_{xx} + C_{yy}Z^{\mathrm{R}}_{yx} & C_{yx}Z^{\mathrm{R}}_{xy} + C_{yy}Z^{\mathrm{R}}_{yy} \end{bmatrix}
\end{aligned} \tag{2.25}$$

where the distortion operator $\mathbf{C}$ is a 2×2 matrix, the elements C_{xx} C_{xy} C_{yx} C_{yy} are real-valued and frequency-independent scalars.

Several attempts have been made to handle the galvanic distortion problem. Here we briefly summarize some of them. The nature of solving the problem of galvanic distortion is an underdetermined problem. Some constraints or assumptions are necessary. For example, the tensor decomposition methods (e.g., Groom and Bailey, 1989; Chave and Smith, 1994; Smith, 1995; McNeice and Jones, 2001) is viable under the assumption of 2D regional structure. Gómez-Treviño et al. (2014) proposed the solution with the aid of rotational invariants, but it is limited to 2D. Ideally, Utada and Munekane (2000) introduced the constraints from Faraday's law, but it is impractical in reality. The phase tensor (Caldwell et al., 2004) and the vertical magnetic transfer function galvanic distortion-free solution. However, because of their absence of magnitude, the inversion based on the phase tensor and the vertical magnetic transfer function strongly depends on the starting models (Siripunvaraporn and Egbert, 2009; Patro et al., 2013; Tietze et al., 2015). Also, the vertical magnetic transfer function or tipper is another galvanic distortion-free response. However, the tipper is only sensitive to the lateral contrast in conductivity. Therefore the model inverted from the tipper relies on an intial or *a priori* model. Simultaneous inversion of MT data and galvanic distortion (e.g., Sasaki and Meju, 2006; Jones, 2011; Avdeeva et al., 2015) is also a forthcoming approach. However, its implementation is rather complicated and still it does not

fully solve the problem.

2.3.2 Distortion operator parameterization: Groom–Bailey's framework

The distortion operator $\mathbf{C}$ can be treated in numerous ways. In this work, we adopted the Groom–Baileys' model of galvanic distortion, which is regarded as one of the standard models of galvanic distortion (e.g., Chave and Smith, 1994; McNeice and Jones, 2001; Chave and Jones, 2012). Its principle is briefly described as follows.

Any 2×2 real-valued matrices $\mathbf{M}$ could be represented by the linear combination of the modifined Pauli spin matrices (Spitz, 1985),

$$\mathbf{M} = \alpha_0 \mathbf{\Sigma}_0 + \alpha_1 \mathbf{\Sigma}_1 + \alpha_2 \mathbf{\Sigma}_2 + \alpha_3 \mathbf{\Sigma}_3, \tag{2.26}$$

where the coefficients $\alpha_{i=0,\ldots,3}$ are arbitrary constants. The modifined Pauli spin matrices are

$$\mathbf{\Sigma}_0 = \begin{bmatrix} 1 & 0 \\ 0 & 1 \end{bmatrix}, \quad \mathbf{\Sigma}_1 = \begin{bmatrix} 0 & 1 \\ 1 & 0 \end{bmatrix}, \quad \mathbf{\Sigma}_2 = \begin{bmatrix} 0 & -1 \\ 1 & 0 \end{bmatrix}, \quad \mathbf{\Sigma}_3 = \begin{bmatrix} 1 & 0 \\ 0 & -1 \end{bmatrix}, \tag{2.27}$$

which are mutually orthonormal. Based on these basis matrices, Groom and Bailey (1989) proposed a *physically-based* parameterization of the distortion operator $\mathbf{C}$, which will be referred to as Groom–Bailey's distortion model:

$$\mathbf{C} = g\mathbf{TSA}. \tag{2.28}$$

The positive scalar g is called the site gain. By analogy to deformation theory of materials (Figure 2.3), the matrices $\mathbf{T}$, $\mathbf{S}$ and $\mathbf{A}$ are, respectively, the twist, shear, and splitting (or anisotropy, but later will be referred to splitting only) operators,

which are 2×2 real-valued matrices. They are given by

$$\begin{aligned}
\mathbf{T} &= N_{\mathbf{T}}(\boldsymbol{\Sigma}_0 + t\boldsymbol{\Sigma}_2) = N_{\mathbf{T}} \begin{bmatrix} 1 & -t \\ t & 1 \end{bmatrix}, \\
\mathbf{S} &= N_{\mathbf{S}}(\boldsymbol{\Sigma}_0 + e\boldsymbol{\Sigma}_1) = N_{\mathbf{S}} \begin{bmatrix} 1 & e \\ e & 1 \end{bmatrix}, \\
\mathbf{A} &= N_{\mathbf{A}}(\boldsymbol{\Sigma}_0 + s\boldsymbol{\Sigma}_3) = N_{\mathbf{A}} \begin{bmatrix} 1+s & 0 \\ 0 & 1-s \end{bmatrix},
\end{aligned} \tag{2.29}$$

where t, e, and s are twist, shear, and splitting parameters; $N_{\mathbf{T}}$, $N_{\mathbf{S}}$, and $N_{\mathbf{A}}$ are the normalizing coefficients defined from the Frobenius norm of each distortion operator (also see Bibby et al., 2005):

$$N_{\mathbf{T}} = \frac{1}{\sqrt{1+t^2}}, \quad N_{\mathbf{S}} = \frac{1}{\sqrt{1+e^2}} \quad \text{and} \quad N_{\mathbf{A}} = \frac{1}{\sqrt{1+s^2}}. \tag{2.30}$$

These normalizing coefficients are introduced to ensure that the power of the distorted electric fields is conserved.

The twist and shear parameters, t and e, can be physically represented by the twist and shear angles:

$$\begin{aligned}
t &= \tan\phi_t \\
e &= \tan\phi_e
\end{aligned} \tag{2.31}$$

By substituting the definitions of twist, shear, and splitting operators (Eq. 2.29) into Eq. (2.28), the explicit form of the distortion operator $\mathbf{C}$ in terms

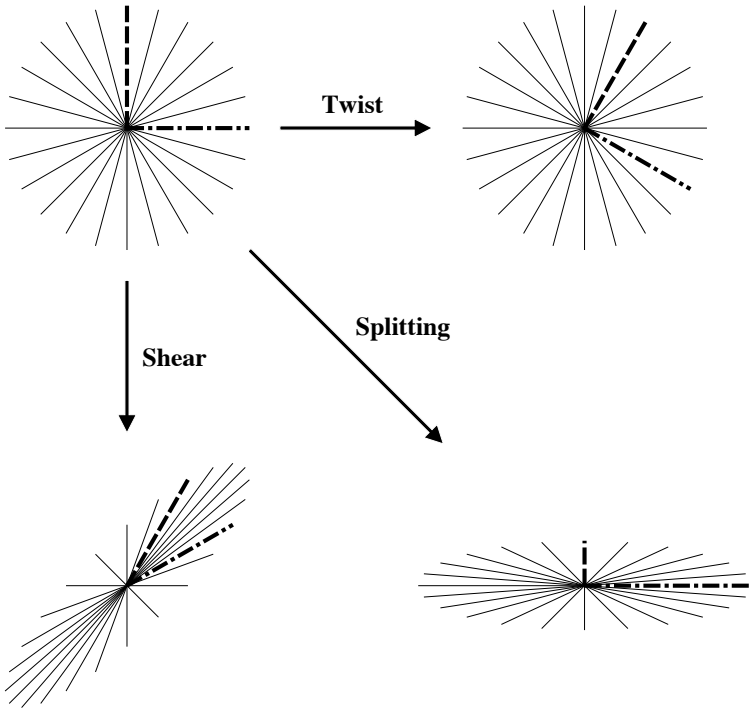

Figure 2.3: Effect of twist, shear and anisotropy operators on a family of unity vectors, where the twist shear and splitting parameters are $\tan 30^\circ$ (after Groom and Bailey, 1989).

of Groom–Bailey's distortion parameters is:

$$\mathbf{C} = \begin{bmatrix} C_{xx} & C_{xy} \\ C_{yx} & C_{yy} \end{bmatrix} = gN_{\mathbf{T}}N_{\mathbf{S}}N_{\mathbf{A}} \begin{bmatrix} (1+s)(1-te) & (1-s)(e-t) \\ (1+s)(e+t) & (1-s)(1+te) \end{bmatrix}. \tag{2.32}$$

The distorted impedance could be calculated by substituting the distortion operator as expressed in Eq. (2.32) into Eq. (2.25). We can also write the the distortion operator $\mathbf{C}$ as a linear combination of the modified Pauli spin matrices:

$$\mathbf{C} = c_0\boldsymbol{\Sigma}_0 + c_1\boldsymbol{\Sigma}_1 + c_2\boldsymbol{\Sigma}_2 + c_3\boldsymbol{\Sigma}_3, \tag{2.33}$$

where the coefficients c_i are:

$$\begin{aligned} c_0 &= g\, N_{\mathbf{T}} N_{\mathbf{S}} N_{\mathbf{A}}\, (1 - est), \\ c_1 &= g\, N_{\mathbf{T}} N_{\mathbf{S}} N_{\mathbf{A}}\, (e + st), \\ c_2 &= g\, N_{\mathbf{T}} N_{\mathbf{S}} N_{\mathbf{A}}\, (es + t), \\ c_3 &= g\, N_{\mathbf{T}} N_{\mathbf{S}} N_{\mathbf{A}}\, (s - et). \end{aligned} \tag{2.34}$$

It is also important to note that the distortion operators – $g, \mathbf{T}, \mathbf{A}$ and $\mathbf{S}$ – act differently on the impedance tensors (Figure 2.3). The site gain g is a scalar. Hence the magnitude of the impedance tensor will be scaled up or down. The effect of site gain g is then called the *static shift* – frequency independent variation in the magnitude, or apparent resistivity, MT data. The twist, shear, and splitting operators, cause the geometrical change, changing the dimensionality of the impedance tensor, and the mixing among components of impedance tensor or called *phase mixing*.

CHAPTER III
ESTIMATING THE REGIONAL MEAN CONDUCTIVITY PROFILE

In addition to the definition of the theoretical model of regional 1D conductivity profile (Eqs. 1.5 and 1.6), we describe the methods proposed in this thesis. First, we showed our finding that the ssq impedance is less sensitive to galvanic distortion when compared to the det impedance. Then, we reexamine the Berdichevsky average and redefine it with the ssq impedance. Lastly, we propose the galvanic distortion-related indicators – the local and regional distortion indicators, and the apparent gains.

3.1 Effect of galvanic distortion on the rotational invariants: Algebraic derivation

In addition to the simple model of galvanic distortion over the det impedance by Berdichevsky et al. (1980), Gómez-Treviño et al. (2013) studied the effect of Groom–Bailey distortion parameters on the det and ssq impedances, but the study was limited to the 2D Earth. In this section, we provide the algebraic derivation of the distorted det and ssq impedances within the Groom–Bailey framework in the general case. The expressions of the distorted det and ssq impedances in Rung-Arunwan et al. (2016) are clarified and derived in terms of the matrix operation which is simple and intuitive.

3.1.1 Distorted det impedance

The determinant of the distorted impedance tensor is straightforward to derive by employing the multiplicative property of determinants. First, we begin

with the generalized form Eq. (2.25),

$$\begin{aligned} \det(\mathbf{Z}') &= \det(\mathbf{C}\,\mathbf{Z}_{\mathrm{R}}) \\ &= \det(\mathbf{C})\det(\mathbf{Z}_{\mathrm{R}}). \end{aligned} \tag{3.1}$$

Applying the Groom–Bailey framework, Eq. (3.1) becomes

$$\begin{aligned} \det(\mathbf{Z}') &= \det(g\mathbf{TSA})\det(\mathbf{Z}_{\mathrm{R}}) \\ &= g^2\det(\mathbf{T})\det(\mathbf{S})\det(\mathbf{A})\det(\mathbf{Z}_{\mathrm{R}}) \\ &= g^2\frac{1-e^2}{1+e^2}\frac{1-s^2}{1+s^2}\det(\mathbf{Z}_{\mathrm{R}}). \end{aligned} \tag{3.2}$$

From Eq. (2.10), the distorted det impedances is then written as

$$Z'_{\mathrm{det}} = g\sqrt{\frac{1-e^2}{1+e^2}\frac{1-s^2}{1+s^2}}\,Z^{\mathrm{R}}_{\mathrm{det}}. \tag{3.3}$$

Evidently, the distorted det impedance is biased downward by the splitting and shear parameters:

$$|Z'_{\mathrm{det}}| = g\sqrt{\frac{1-e^2}{1+e^2}\frac{1-s^2}{1+s^2}}\,|Z^{\mathrm{R}}_{\mathrm{det}}| \le g\,|Z^{\mathrm{R}}_{\mathrm{det}}| \tag{3.4}$$

Hence, using the det impedance may result in an underestimating the regional impedance by the shear and splitting effects.

From Eqs. (3.1) and (3.2), the effect of galvanic distortion on the det impedance causes only the impedance scaling. The expression in Eq. (3.3) also clarifies the coefficient K_i, which have no definition but the random quantity, in the galvanic distortion model of Berdichevsky et al. (1980) (Eq. 2.12).

The virtue of using the det impedance is that its phase is distortion free, regardless of dimensionality of the earth. However, it may be problematic because the effect of site gain and splitting and shear parameters are indistinguishable. All of them can cause the shift in det apparent resistivity.

3.1.2 Distorted ssq impedance

Owing to the Frobenius norm definition of the normalizing coefficients, $N_{\mathbf{T}}N_{\mathbf{S}}N_{\mathbf{A}}$, and the Frobenius norm-like definition of ssq impedance, we are interested in examining the ssq impedance under galvanic distortion. As with the previous subsection, we begin deriving the distorted ssq in the generalized form of the distortion operator and then apply Groom–Bailey decomposition. The ssq of the distorted impedance tensor could be obtained by performing straightforward algebra, but here we chose to use the matrix operation.

Starting from the product of the distorted impedance tensor,

$$\begin{aligned}
\mathbf{Z'}^{\mathrm{T}}\mathbf{Z'} &= \mathbf{Z}_{\mathrm{R}}{}^{\mathrm{T}}\mathbf{C}^{\mathrm{T}}\mathbf{C}\mathbf{Z}_{\mathrm{R}} \\
&= \mathbf{Z}_{\mathrm{R}}{}^{\mathrm{T}}(c_0\mathbf{\Sigma}_0 + c_1\mathbf{\Sigma}_1 + c_2\mathbf{\Sigma}_2 + c_3\mathbf{\Sigma}_3)^{\mathrm{T}}(c_0\mathbf{\Sigma}_0 + c_1\mathbf{\Sigma}_1 + c_2\mathbf{\Sigma}_2 + c_3\mathbf{\Sigma}_3)\mathbf{Z}_{\mathrm{R}} \\
&= \mathbf{Z}_{\mathrm{R}}{}^{\mathrm{T}}\left[\left(c_0^2 + c_1^2 + c_2^2 + c_3^2\right)\mathbf{\Sigma}_0 + 2\left(c_0c_3 + c_1c_2\right)\mathbf{\Sigma}_3 + 2\left(c_0c_1 - c_2c_3\right)\mathbf{\Sigma}_1\right]\mathbf{Z}_{\mathrm{R}}
\end{aligned} \tag{3.5}$$

Calculating trace of Eq. (3.5) to get the ssq of the distorted impedance tensor,

$$\begin{aligned}
\mathrm{ssq}(\mathbf{Z'}) &= \mathrm{tr}(\mathbf{Z}_{\mathrm{R}}{}^{\mathrm{T}}\mathbf{C}^{\mathrm{T}}\mathbf{C}\mathbf{Z}_{\mathrm{R}}) \\
&= \left(c_0^2 + c_1^2 + c_2^2 + c_3^2\right)\mathrm{tr}(\mathbf{Z}_{\mathrm{R}}{}^{\mathrm{T}}\mathbf{Z}_{\mathrm{R}}) \\
&\quad + 2\left(c_0c_3 + c_1c_2\right)\mathrm{tr}(\mathbf{Z}_{\mathrm{R}}{}^{\mathrm{T}}\mathbf{\Sigma}_3\mathbf{Z}_{\mathrm{R}}) \\
&\quad + 2\left(c_0c_1 - c_2c_3\right)\mathrm{tr}(\mathbf{Z}_{\mathrm{R}}{}^{\mathrm{T}}\mathbf{\Sigma}_1\mathbf{Z}_{\mathrm{R}}) \\
&= \left(c_0^2 + c_1^2 + c_2^2 + c_3^2\right)\mathrm{ssq}(\mathbf{Z}_{\mathrm{R}}) \\
&\quad + 2\left(c_0c_3 + c_1c_2\right)\left(Z_{xx}^{\mathrm{R}\,2} + Z_{xy}^{\mathrm{R}\,2} - Z_{yx}^{\mathrm{R}\,2} - Z_{yy}^{\mathrm{R}\,2}\right) \\
&\quad + 2\left(c_0c_1 - c_2c_3\right)\,2(Z_{xx}^{\mathrm{R}}Z_{yx}^{\mathrm{R}} + Z_{xy}^{\mathrm{R}}Z_{yy}^{\mathrm{R}})
\end{aligned} \tag{3.6}$$

Note that Eq. (3.6) is free of $\mathbf{\Sigma}_2$, which defines the twist operator. Substituting the coefficients c_i in Eq. (2.34) into Eq. (3.6) and perfoming modest algebra, we

obtain:

$$\begin{aligned}\mathrm{ssq}(\mathbf{Z}') = g^2 N_{\mathbf{T}}^2 N_{\mathbf{S}}^2 N_{\mathbf{A}}^2 (1+t^2)(1+e^2)(1+s^2) \Bigg[& \\ \mathrm{ssq}(\mathbf{Z}_{\mathrm{R}}) + \frac{2s}{(1+s^2)}(Z_{xx}^{\mathrm{R}\,2} + Z_{xy}^{\mathrm{R}\,2} - Z_{yx}^{\mathrm{R}\,2} - Z_{yy}^{\mathrm{R}\,2}) & \\ + \frac{4e\,(1-s^2)}{(1+e^2)(1+s^2)}(Z_{xx}^{\mathrm{R}} Z_{yx}^{\mathrm{R}} + Z_{xy}^{\mathrm{R}} Z_{yy}^{\mathrm{R}})\Bigg] & \\ = g^2 \Bigg[\mathrm{ssq}(\mathbf{Z}_{\mathrm{R}}) + \frac{2s}{(1+s^2)}(Z_{xx}^{\mathrm{R}\,2} + Z_{xy}^{\mathrm{R}\,2} - Z_{yx}^{\mathrm{R}\,2} - Z_{yy}^{\mathrm{R}\,2}) & \\ + \frac{4e\,(1-s^2)}{(1+e^2)(1+s^2)}(Z_{xx}^{\mathrm{R}} Z_{yx}^{\mathrm{R}} + Z_{xy}^{\mathrm{R}} Z_{yy}^{\mathrm{R}})\Bigg] & \end{aligned} \tag{3.7}$$

The effect of the distortion parameters on the ssq impedance depends on the dimensionality of the structure. The splitting parameter will be effective if the Earth is not 1D (the 2nd and 3rd terms in Eq. 3.7), while the shear parameter becomes effective when the Earth is 3D only (the 3rd term in Eq. 3.7). Note that Gómez-Treviño et al. (2013) also obtained the expression similar to Eq. (3.7).

As with the det impedance, the ssq impedance is the rotational invariant and hence independent of the twist parameter. Adopting Eq. (2.11), for simplicity we write the distorted ssq impedance:

$$Z'_{\mathrm{ssq}} = g Z^{\dagger}_{\mathrm{ssq}}, \tag{3.8}$$

where

$$\begin{aligned} Z^{\dagger}_{\mathrm{ssq}} = \frac{1}{\sqrt{2}} \Bigg[\mathrm{ssq}(\mathbf{Z}_{\mathrm{R}}) + \frac{2s}{(1+s^2)}(Z_{xx}^{\mathrm{R}\,2} + Z_{xy}^{\mathrm{R}\,2} - Z_{yx}^{\mathrm{R}\,2} - Z_{yy}^{\mathrm{R}\,2}) & \\ + \frac{4e\,(1-s^2)}{(1+e^2)(1+s^2)}(Z_{xx}^{\mathrm{R}} Z_{yx}^{\mathrm{R}} + Z_{xy}^{\mathrm{R}} Z_{yy}^{\mathrm{R}})\Bigg]^{\frac{1}{2}} & \end{aligned} \tag{3.9}$$

3.2 Redefining the Berdichevsky average

Although using the ssq impedance may reduce the bias due to the splitting and shear parameters, the site gain g remains the problem. In this section,

we will show that the average approach is one strategy to relieve the problem of site gain. Also, to show the difference between using the average det impedance and the average ssq impedance, we reexamine the Berdichevsky average within the Groom–Bailey framework, and redefine the Berdichevsky average with the ssq impedance.

Given that N MT observations were made, we rewrite the Berdichevsky average (Eq. 2.13) as the geometric average of impedances,

$$\bar{Z}'_{\mathrm{det}}(\omega) = \left[\prod_{i=1}^{N} Z'_{\mathrm{det}}(\mathbf{r}_i;\omega)\right]^{\frac{1}{N}}, \tag{3.10}$$

where $\mathbf{r}_i$ denotes the position vector of the ith observation. Substituting the distorted det impedance Eq. (3.3) into Eq. (3.10),

$$\bar{Z}'_{\mathrm{det}}(\omega) = \left[\prod_{i=1}^{N} g_i \sqrt{\frac{1-e_i^2}{1+e_i^2}\frac{1-s_i^2}{1+s_i^2}}\, Z^{\mathrm{R}}_{\mathrm{det}}(\mathbf{r}_i;\omega)\right]^{\frac{1}{N}}, \tag{3.11}$$

where g_i, e_i and s_i are the site gain, shear and splitting parameters at the ith station. On the basis of the central limit theorem and assuming that the site gain is log-normally distributed (Berdichevsky et al., 1980), the arithmetic average of site gains from a number of observations in a logarithmic scale is approximately zero (see also DeGroot-Hedlin, 1991; Ogawa et al., 1996). In other words, the geometric average of site gains becomes unity:

$$\prod_{i=1}^{N} g_i \to 1. \tag{3.12}$$

Approximately, the average det impedance then becomes

$$\begin{aligned}\bar{Z}'_{\mathrm{det}}(\omega) &\approx \left[\prod_{i=1}^{N} \sqrt{\frac{1-e_i^2}{1+e_i^2}\frac{1-s_i^2}{1+s_i^2}}\, Z^{\mathrm{R}}_{\mathrm{det}}(\mathbf{r}_i;\omega)\right]^{\frac{1}{N}} \\ &\approx \left[\prod_{i=1}^{N} \sqrt{\frac{1-e_i^2}{1+e_i^2}\frac{1-s_i^2}{1+s_i^2}}\right]^{\frac{1}{N}} \bar{Z}^{\mathrm{R}}_{\mathrm{det}}(\omega),\end{aligned} \tag{3.13}$$

where the average regional det impedance

$$\bar{Z}^{\mathrm{R}}_{\mathrm{det}}(\omega) = \left[\prod_{i=1}^{N} Z^{\mathrm{R}}_{\mathrm{det}}(\mathbf{r}_i;\omega)\right]^{\frac{1}{N}}. \tag{3.14}$$

Averaging the impedance and applying the central limit theorem would help relieve the problem of site gain. However, the remaining coefficient of splitting and shear parameters, which is always less than unity, will underestimate the regional det impedance in terms of apparent resistivity. In other words, the Berdichevsky average may lead to an overestimated model of the regional mean 1D conductivity profile. However, Baba et al. (2010) successfully applied the Berdichevsky average to marine MT data after showing that the galvanic distortion is negligible.

Next, we redefine the Berdichevsky average with the ssq impedance. As the ssq impedance is less sensitive to the distortion parameters, the average ssq impedance is expected to yield the reliable estimate of the regional mean 1D conductivity profile. Writing the average ssq impedance as

$$\bar{Z}'_{\mathrm{ssq}}(\omega) = \left[\prod_{i=1}^{N} Z'_{\mathrm{ssq}}(\mathbf{r}_i;\omega)\right]^{\frac{1}{N}}. \tag{3.15}$$

and substituting the distorted ssq impedance (Eq. 3.8) into Eq. (3.15) gives

$$\bar{Z}'_{\mathrm{ssq}}(\omega) = \left[\prod_{i=1}^{N} g_i\, Z^{\dagger}_{\mathrm{ssq}}(\mathbf{r}_i;\omega)\right]^{\frac{1}{N}}. \tag{3.16}$$

As with Eq. (3.13), the central limit theorem is applied in averging site gain. If we average the impedance from a large number of observations covering an sufficiently large area, we may assume the effect of the 2nd and 3rd terms in Eq. (3.9) becomes negligible. The average ssq impedance (Eq. 3.16) becomes

$$\bar{Z}'_{\mathrm{ssq}}(\omega) \approx \bar{Z}^{\mathrm{R}}_{\mathrm{ssq}}(\omega), \tag{3.17}$$

where the average regional ssq impedance

$$\bar{Z}^{\mathrm{R}}_{\mathrm{ssq}}(\omega) = \left[\prod_{i=1}^{N} Z^{\mathrm{R}}_{\mathrm{ssq}}(\mathbf{r}_i;\omega)\right]^{\frac{1}{N}}. \tag{3.18}$$

Therefore, the average ssq impedance would give the good estimate of the regional mean 1D conductivity profile.

3.3 Indicating the galvanic distortion

In addition to estimating the regional mean conductvity profile, the combination of the det and ssq impedances would help determine the existence and strength of galvanic distortion contained in an MT dataset.

3.3.1 Local and regional distortion indicators

Employing the fact that the effect of galvanic distortion on the det and ssq impedances are different, the local distortion indicator is defined as the squared ratio of the det impedance to the ssq impedance

$$\gamma_i(\omega) = \frac{Z'_{\mathrm{ssq}}(\mathbf{r}_i;\omega)^2}{Z'_{\mathrm{det}}(\mathbf{r}_i;\omega)^2}. \tag{3.19}$$

Applying the expressions for Z'_{ssq} and Z'_{det} in Eqs. (3.3) and (3.8), we obtain

$$\gamma_i(\omega) = \frac{g_i^2\, Z^{\dagger}_{\mathrm{ssq}}(\mathbf{r}_i;\omega)^2}{g_i^2\, \dfrac{1-e_i^2}{1+e_i^2}\dfrac{1-s_i^2}{1+s_i^2}\, Z^{\mathrm{R}}_{\mathrm{det}}(\mathbf{r}_i;\omega)^2}. \tag{3.20}$$

The presence of galvanic distortion can be examined by the consistency between the vertical magnetic transfer function and the lateral gradients of MT impedance (Utada and Munekane, 2000; Rung-Arunwan et al., 2016). The importance of the local distortion indicator exists in the separation of the site gain.

In general cases, we may approximate the local distortion indicator as:

$$\gamma_i(\omega) \approx \frac{1+e_i^2}{1-e_i^2}\frac{1+s_i^2}{1-s_i^2}\frac{Z^{\mathrm{R}}_{\mathrm{ssq}}(\mathbf{r}_i;\omega)^2}{Z^{\mathrm{R}}_{\mathrm{det}}(\mathbf{r}_i;\omega)^2} \approx \frac{1+e_i^2}{1-e_i^2}\frac{1+s_i^2}{1-s_i^2}. \tag{3.21}$$

The local distortion indicator is expressed as the product of the coefficient of distortion parameters and the difference between the ssq and det impedances. The former is real-valued and frequency independent, and larger than unity if the data is distorted, while the latter is generally complex-valued and frequency-dependent. The difference between the det and ssq impedances is generally small; consequently, it may be ignored. In an 1D situation, the local distortion indicator becomes

$$\gamma_i = \frac{1+e_i^2}{1-e_i^2}\frac{1+s_i^2}{1-s_i^2}. \tag{3.22}$$

This ratio is the real-valued number indicating the strength of shear and splitting parameters. The stronger the galvanic distortion, the greater the local distortion indicator. But if there is no distortion, the local distortion indicator becomes unity in the 1D situation.

In general, if the local distortion indicator was found to be real-valued and weakly frequency independent, the 1D regional structure may be assumed. The magnitude of the local distortion indicator denotes the strength of galvanic distortion posed in the data. If the local distortion indicator is varied (frequency dependent) about some constant magnitude, the distorted 3D data is suggested.

Further, we also define the mean local distortion indicator $\bar{\gamma}_i$ by averaging the local distortion indicator over the given period range so as to relieve the frequency dependent part, which is mainly due to the underlying structure. Given that at the ith stations the number of periods is M, the mean local distortion indicator is given by averaging the real part of the local distortion indicator:

$$\bar{\gamma}_i = \left[\prod_{j=1}^{M} \Re\, \gamma_i(\omega_j)\right]^{\frac{1}{M}}. \tag{3.23}$$

Only the real part is used in order to conform with the assumption that the galvanic

distortion operator is real. This single-valued parameter is able to represent the galvanic distortion strength at an MT station and also ease analysing data from a number of MT stations.

In addition to the local distortion indicator (Eq. 3.19), we can determine how strongly the dataset is distorted using the regional distortion indicator, which is defined as the geometric mean of the local distortion indicators:

$$\gamma_{\mathrm{R}}(\omega) = \left[\prod_{i=1}^{N} \gamma_i(\omega)\right]^{\frac{1}{N}} \tag{3.24}$$

Substituting the approximation in Eq. (3.13) into Eq. (3.17), we get

$$\begin{aligned} \gamma_{\mathrm{R}}(\omega) &\approx \left[\prod_{i=1}^{N} \frac{1+e_i^2}{1-e_i^2}\frac{1+s_i^2}{1-s_i^2}\right]^{\frac{1}{N}} \frac{\bar{Z}^{\mathrm{R}}_{\mathrm{ssq}}(\mathbf{r}_i;\omega)^2}{\bar{Z}^{\mathrm{R}}_{\mathrm{det}}(\mathbf{r}_i;\omega)^2} \\ &\approx \left[\prod_{i=1}^{N} \frac{1+e_i^2}{1-e_i^2}\frac{1+s_i^2}{1-s_i^2}\right]^{\frac{1}{N}} . \end{aligned} \tag{3.25}$$

By averaging the local distortion indicators, the contribution of the difference between the ssq and det impedances is diminished. The regional distortion indicator is expected to be real and frequency independent, and its magnitude represents the effect of the shear and splitting parameters on average. As with the local distortion indicator, the larger the magnitude of the regional distortion indicator, the stronger the galvanic distortion. In some areas, if the near-surface layer is highly heterogenous, strong galvanic distortion is expected and the regional distortion indicator would help quantify its strength. If the MT dataset is strongly distorted, the proper treatment or removal of galvanic distortion may be necessary.

3.3.2 Apparent gains

In addition to determining the strength of the shear and splitting parameters, the apparent gain was introduced to determine the magnitude of site gain, which generally claimed to be undeterminable without other independent information (Groom et al., 1993; Bibby et al., 2005). Here we show that estimating

the site gain is plausible from a set of MT data.

As the averaging approach and assuming the central limit theorem relieves the problem of site gain, the apparent gains could be defined from the ratio of individual invariant impedance to the average impedance. As two rotational invariants are of interest, we then examine two apparent gains, the apparent det and ssq gains:

$$g_i^{\det}(\omega) = \frac{Z'_{\det}(\mathbf{r}_i;\omega)}{\bar{Z}'_{\det}(\omega)} \tag{3.26}$$

and

$$g_i^{\mathrm{ssq}}(\omega) = \frac{Z'_{\mathrm{ssq}}(\mathbf{r}_i;\omega)}{\bar{Z}'_{\mathrm{ssq}}(\omega)}. \tag{3.27}$$

In the 1D Earth, we will have

$$g_i^{\det} = g_i \sqrt{\frac{1-e_i^2}{1+e_i^2}\frac{1-s_i^2}{1+s_i^2}} \Bigg/ \left[\prod_{i=1}^{N} \sqrt{\frac{1-e_i^2}{1+e_i^2}\frac{1-s_i^2}{1+s_i^2}}\right]^{\frac{1}{N}} \tag{3.28}$$

and

$$g_i^{\mathrm{ssq}} = g_i \tag{3.29}$$

If the apparent det and ssq gains are real and almost frequency independent, we may assume the earth is likely 1D. The magnitude of the apparent ssq gain would give a good estimate of the actual site gain.

In general, the apparent det gain is obtained by substituting the expressions for $Z'_{\det}$ and $\bar{Z}'_{\det}$ (Eqs. 3.3 and 3.13) into Eq. (3.26):

$$\begin{aligned} g_i^{\det}(\omega) &\approx g_i \sqrt{\frac{1-e_i^2}{1+e_i^2}\frac{1-s_i^2}{1+s_i^2}}\, Z^{\mathrm{R}}_{\det}(\mathbf{r}_i;\omega) \Bigg/ \left[\prod_{i=1}^{N} \sqrt{\frac{1-e_i^2}{1+e_i^2}\frac{1-s_i^2}{1+s_i^2}}\right]^{\frac{1}{N}} \bar{Z}^{\mathrm{R}}_{\det}(\omega) \\ &\approx g_i \sqrt{\frac{1-e_i^2}{1+e_i^2}\frac{1-s_i^2}{1+s_i^2}} \Bigg/ \left[\prod_{i=1}^{N} \sqrt{\frac{1-e_i^2}{1+e_i^2}\frac{1-s_i^2}{1+s_i^2}}\right]^{\frac{1}{N}}. \end{aligned} \tag{3.30}$$

The apparent ssq gain is obtained by substituting the expressions for Z'_{ssq} and $\bar{Z}'_{\mathrm{ssq}}$

(Eqs. 3.8 and 3.17) into Eq. (3.27):

$$\begin{aligned} g_i^{\text{ssq}}(\omega) &\approx g_i Z_{\text{ssq}}^{\dagger}(\mathbf{r}_i;\omega) \Big/ \bar{Z}_{\text{ssq}}^{\text{R}}(\omega) \\ &\approx g_i \end{aligned} \tag{3.31}$$

Whether the Earth is 1D or not, the shear and splitting parameters systematically affect the apparent det gain. If the distortion at the individual station is stronger than the average, the apparent det gain will underestimate the actual site gain. Therefore the apparent det gain is either an overestimate or an underestimate.

To estimate the site gain for each station, we propose to calculate the mean apparent det and ssq gains $\bar{g}_i^{\text{det}}$ and $\bar{g}_i^{\text{ssq}}$ by averaging the real part of the apparent gains over the period range of interest. Given that at each stations the number of periods is M, the mean apparent gains are:

$$\bar{g}_i^{\text{det}} = \left[\prod_{j=1}^{M} \Re\, g_i^{\text{det}}(\omega_j) \right]^{\frac{1}{M}} \tag{3.32}$$

and

$$\bar{g}_i^{\text{ssq}} = \left[\prod_{j=1}^{M} \Re\, g_i^{\text{ssq}}(\omega_j) \right]^{\frac{1}{M}} \tag{3.33}$$

Averaging would help flatten the frequency dependent features due to the underlying heterogeneity. The mean apparent ssq gain are expected to be a good estimate of the site gain.

CHAPTER IV
SYNTHETIC EXPERIMENTS AND DISCUSSION

In this chapter, we test the proposed methods (as described in Chapter 3) using the average ssq impedance to estimate the regional mean 1D conductivity profile and deriving galvanic distortion-related indicators through synthetic examples. Synthetic 1D and 3D models are used, and the galvanic distortion was simulated with the random distortion parameters – g, t, e and s. As we introduce the theoretical model of regional mean 1D conductivity profile (Eqs. 1.5 and 1.6), we examined if it is consistent with the model of regional mean 1D conductivity profile estimated from the average ssq impedance.

4.1 Estimating a model of regional mean 1D profile: 1D example

In this work, the synthetic layered-Earth model (Figure 4.1a) was made based on Jones (1999), which has the main feature of resistive upper crust (3.5–14.8 km depth) and conductive lower crust (14.8–33.3 km depth). This feature is commonly found in the continental crust (Jones, 1999). The corresponding MT response was calculated in the period range of (Figure 4.1) using the analytic solution (Constable et al., 1987). The heterogeneity embedded in the lower crust layer is detectable in this period range, while any structures confined in the near-surface layer – a few kilometers or less, which is shallower and thinner than the inductive scale length of interest – are considered to be the galvanic distorters.

As described earlier, the near-surface distorters cause spatial aliasing in the data. The distortion parameters in the Groom–Bailey framework – site gain g, twist t, shear e and splitting s parameters – can reasonably be assumed to

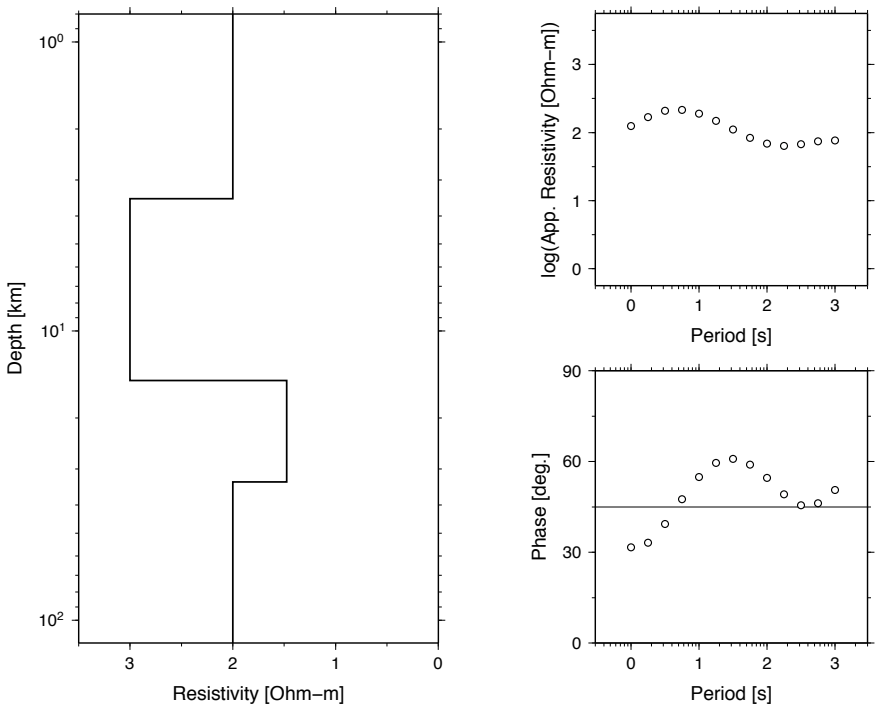

Figure 4.1: (a) Layered-Earth model used in this work. (b) Corresponding MT response (apparent resistivity and phase).

be random (e.g., Avdeeva et al., 2015). Given that the MT array consists of 25 MT stations in our synthetic tests, 25 sets of real-valued parameters (g, t, e, s) are generated from the normal distribution. Also, to quantify the galvanic distortion strength, the standard deviation (SD) used in the normal distribution ranges from 0.1–0.5 (Figure 4.2). Note that when the SD was greater than 0.3, the randomly generated numbers were less likely to comply with the theoretical normal distribution, and more like the uniform distribution. We further assume that each set of distortion parameters has the mean of zero and is within $(-1, +1)$. Note that the random site gain was made in an logarithmic scale. Eventually, we have five MT datasets, 25 stations each, distorted with different galvanic distortion strength. The distorted impedances are calculated using Eq. (2.25) by applying these random parameters to the 1D impedance (as shown in Figure 4.1).

In the 1D Earth, the galvanic distortion causes no phase mixing, but only a static shift in magnitude of the MT components (Figure 4.3a), whereas the galvanic distortion, as proven, only causes the static shift in the rotationally

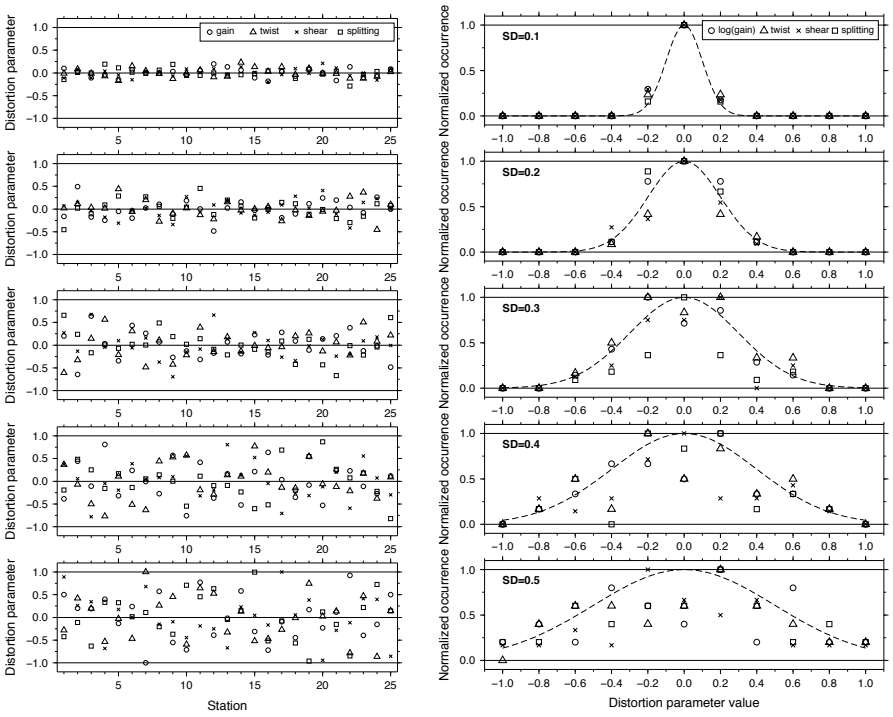

(a) (b)

Figure 4.2: (a) Random distortion parameter values generated from the normal distribution with different SDs. (b) Distribution of the distortion parameters. The normalized occurrence is the number of occurrences divided by the maximum number of occurrences at a single parameter value. Each distribution is compared with the probability density function of the theoretical normal distribution for the given SD (dashed lines).

invariant impedances (Figure 4.3b). The MT data in this example is distorted with (g, t, e, s) of $(1.20, 0.11, -0.37, 0.49)$. In this example, the synthetic site gain g is greater than unity. Therefore the ssq impedance is shifed upward. As described in Section 3.1, the site gain provides the same effect on the det and ssq impedances. Hence the det impedance is also supposed to be shifted upward, but here it is biased downward due to the shear and splitting parameters so that its magnitude is less than the undistorted impedance.

As the distortion parameters are randomly generated, the rotational invariant impedances are irregularly shifted (Figure 4.4), which resembles the results in Berdichevsky et al. (1980) (Figure 2.1). The shift in the ssq impedance is solely due to the site gain, but the shift in the det impedance also includes the shear and splitting parameters. As mentioned, this behaviour could be problem-

atic because the effect of the shear and splitting parameters and the site gain is indistinguishable, if the det impedance is chosen.

To examine the effect of galvanic distortion strength on the regional mean impedance, the average det and ssq impedances for each distorted dataset (Figure 4.5) were calculated using Eqs. (3.10) and (3.15), respectively. Here, the error bar is the standard deviation of the data and therefore represents the level of dispersion of the sounding curves. The large error bars correspond to strong galvanic distortion strengths. For example, the dataset distorted with an SD of 0.5 has the largest error bar. At the same strength of galvanic distortion, the average det impedances appear to be more dispersed than the average ssq impedances, because the shear and splitting parameters also affect the det impedance. From the results, the average det impedance is biased downward by the galvanic distortion, although its effect is not noticeable when the SD of the distortion parameters is less than 0.2. On the contrary, the average ssq impedances remain the same at all galvanic distortion strengths. This is consistent with the theoretical derivation that the average ssq impedance would give the unbiased approximation of the model of the regional mean 1D conductivity profile (Rung-Arunwan et al., 2016).

In this work, the Occam 1D inversion (Constable et al., 1987) is used to yield the 1D models, in which the second derivative of the conductivity with respect to the depth is penalized. The errors of the apparent resistivity and phase applied in the inversion were fixed at 2.3% and 0.66°, respectively. All inverted models shown in this work fit the data within a root mean square (RMS) error of unity. The inverted models from the average det impedances will be less resistive or more conductive than the true structure, particularly when the galvanic distortion is strong. On the other hand, the average ssq impedances give models that are very close to the true structure regardless of galvanic distortion strengths. From the synthetic tests, when the galvanic distortion is included, the true 1D structure may be missed due to the downward-biased det impedance. The average ssq impedances would be the appropriate candidate to estimate the regional mean 1D conductivity profile.

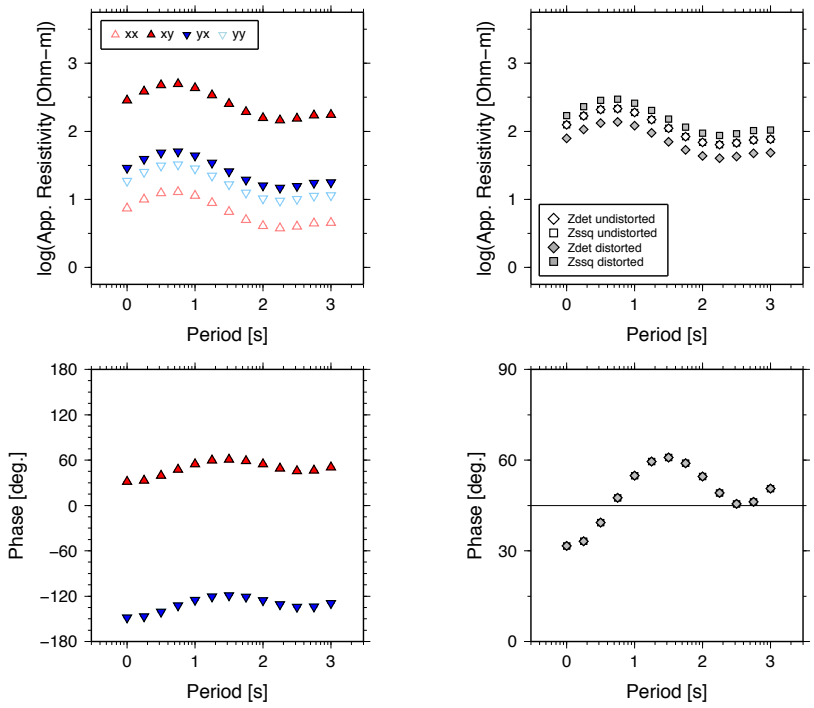

(a) (b)

Figure 4.3: (a) Components of the 1D MT impedance distorted with $(g, t, e, s) = (1.20, 0.11, -0.37, 0.49)$. (b) Corresponding det (diamonds) and ssq (squares) impedances.

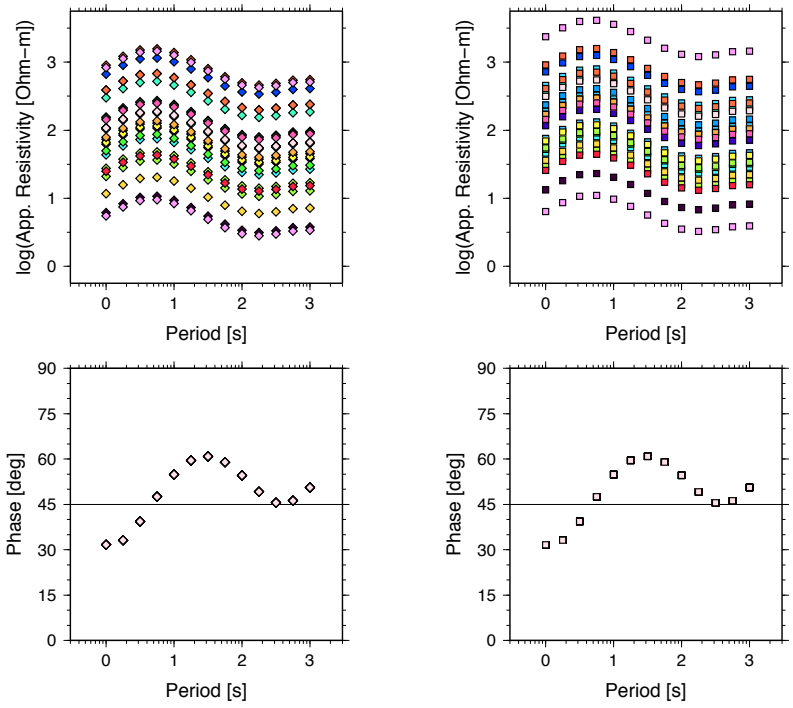

(a) (b)

Figure 4.4: Distorted (a) det and (b) ssq impedances from the 1D example, where a set of distortion parameters with an SD of 0.3 was applied. Each station is represented by a different symbol color.

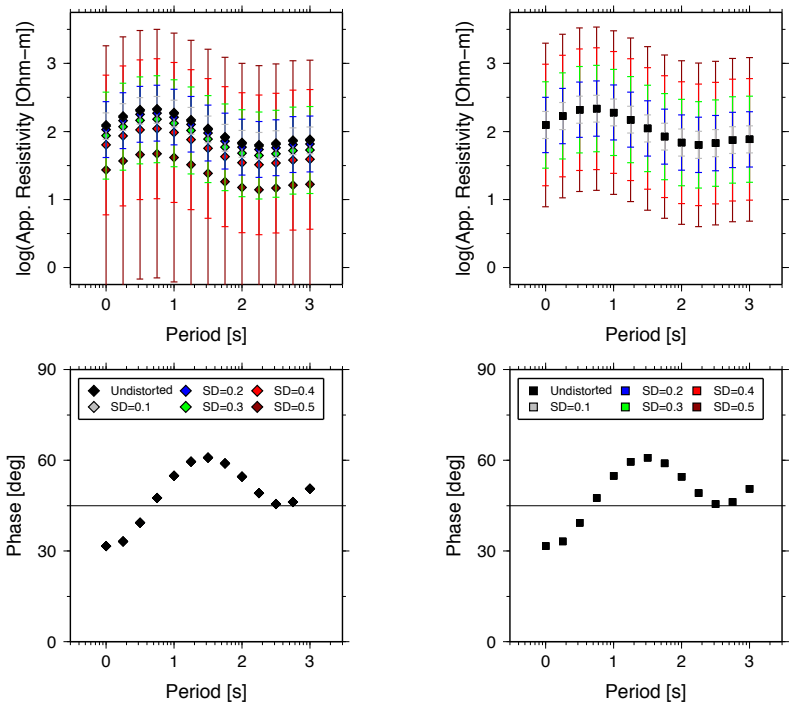

(a) (b)

Figure 4.5: Average (a) det and (b) ssq impedances from the 1D datasets distorted with different galvanic distortion strengths.

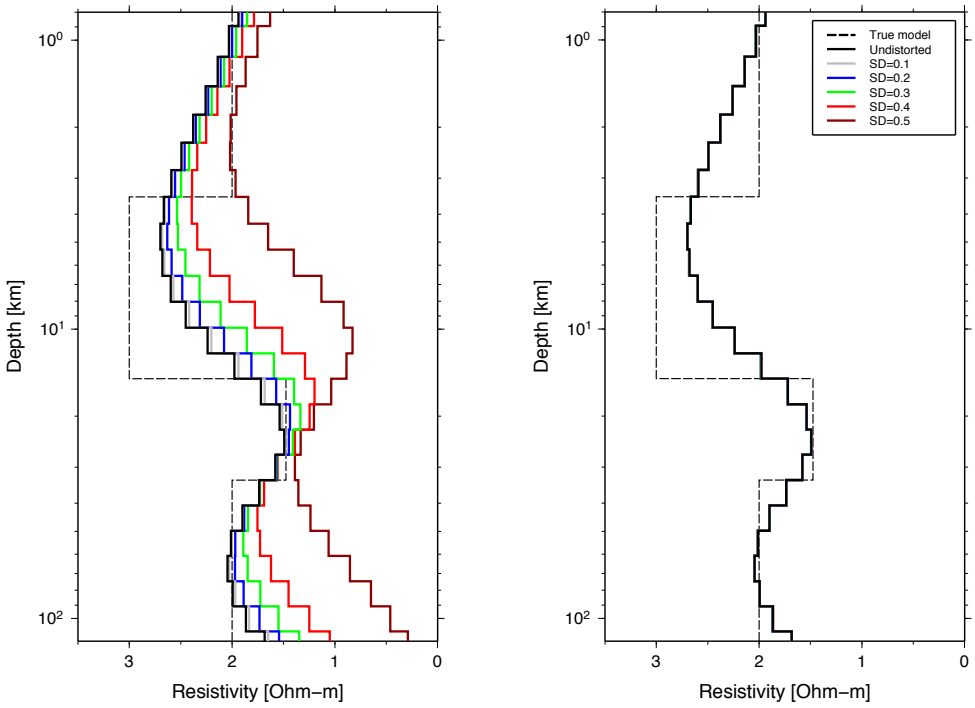

Figure 4.6: 1D models obtained by inverting the average (a) det and (b) ssq impedances from the distorted 1D datasets (Figure 4.5). The true structure (dashed lines) is also shown for comparison.

4.2 Estimating a model of regional mean 1D profile: 3D example

The 3D model used in this work are generated from embedding checkerboard anomalies with resistivities of 3 and 300 Ω m and a size of 40 km × 40 km (Figure 4.7) in the lower crust (14.8–33.3 km depth) of the layered-Earth model as in the 1D example (Figure 4.1a). The anomalies at this depth range could be detectable within the given period range. We can determine the inductive scale length using Eq. (2.20), where the conductivity contrast $\delta\sigma$ is $1/3 - 1/300$ Sm^{-1}. From the shortest to the longest periods (1–1,000 s), the inductive scale lengths corresponding to these anomalies range from 876 m to 27.7 km. They are not much smaller than its physical dimension (40 km × 40 km); therefore, the inductive effect from these anomalies should be sufficient.

The details of the MT array configuration are as follows. The 25 MT stations are distributed over the area of interest which is 80 km × 80 km (Figure 4.7). Consequently, the site spacing is 16 km, i.e., each site represents an area of 16

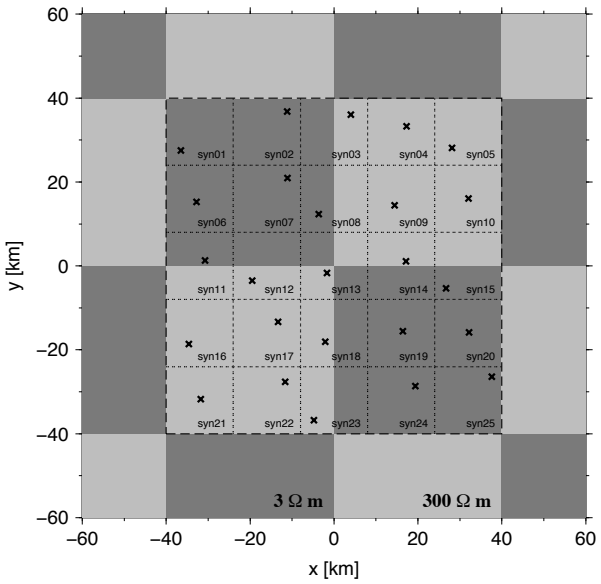

Figure 4.7: Model of checkerboard anomalies with resistivities of 3 and 300 Ω m and a size of 40 km × 40 km embedded in the lower crust layer. The array of 25 irregularly distributed MT stations (crosses) covers the area of interest, which is 80 km × 80 km (dashed frame). Here, one MT station represents an area of 16 km × 16 km (dash-dotted frames).

km × 16 km (1/25 of the area of interest). To simulate the irregularly distributed MT array, the location of the ith station is given by

$$x_i = x_c + sr_x$$
$$y_i = y_c + sr_y,$$

where (x_c, y_c) is the coordinate of the mesh center represented by each MT site; s is the site spacing, which is 16 km in the setup; r_x and r_y are uniform random numbers bounded within $(-0.5, +0.5)$.

The MT responses are calculated using the software WSINV3DMT (Siripunvaraporn et al., 2005). Without galvanic distortion, the static shift is not observed in the det and ssq impedances, and their distributions are also similar (Figure 4.8). The checkerboard anomalies are recognized in the period range of 2–30 s, as seen from the slight variation in the impedances. To obtain the distorted 3D dataset, the set of random distortion parameters as used in the 1D example

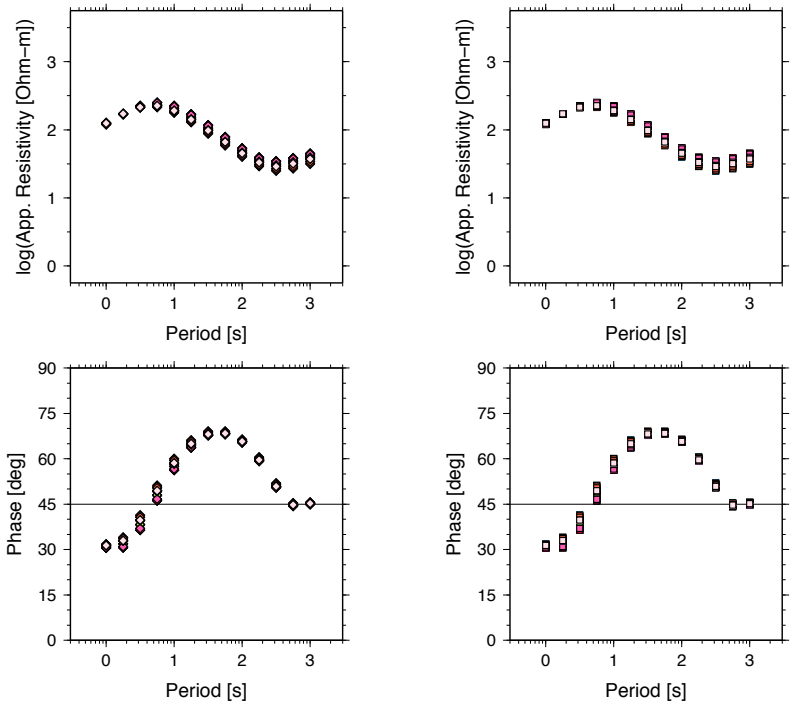

(a) (b)

Figure 4.8: (a) Det and (b) ssq impedances from the array of MT stations over the 3D anomalies. Each station is represented by a different symbol color.

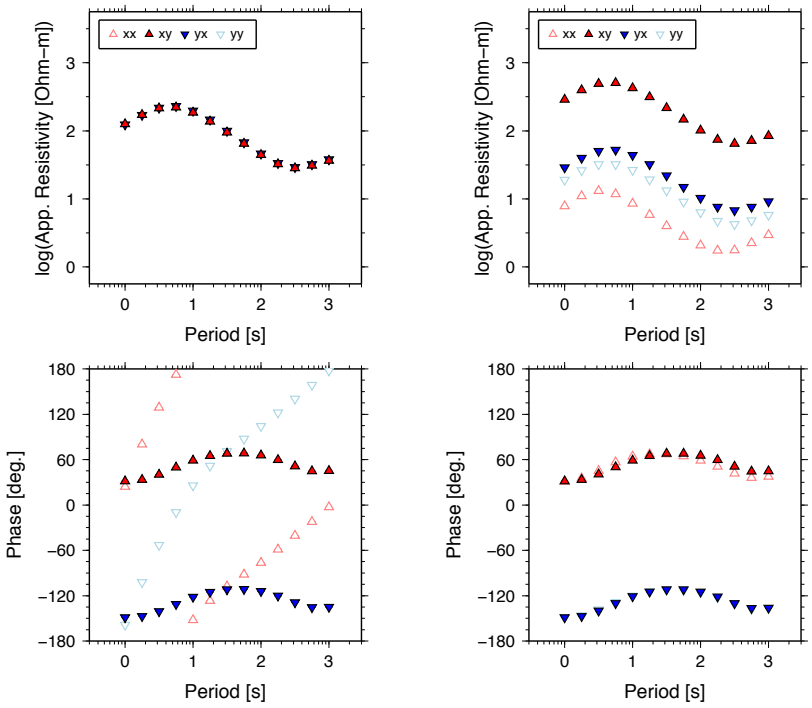

(a) (b)

Figure 4.9: Components of the MT impedance from station `syn08` (a) undistorted and (b) distorted with $(g, t, e, s) = (1.20, 0.11, -0.37, 0.49)$.

were applied to the calculated 3D data using Eq. (2.25). The example of the undistorted MT impedance from the station `syn08` is shown in Figure 4.9a. The magnitudes of the diagonal components – xx and yy – are rather weak. When it is distorted, their magnitudes increase (Figure 4.9b), and the phase mixing, i.e., the frequency dependent feature of the xx phase, can be observed. Unlike the 1D case, the ssq impedance from the distorted impedances is not only shifted, but also contains a weak frequency dependence (Figure 4.10a), which is better observed from the difference of the magnitude and phase between the distorted and undistorted rotational invariants (Figure 4.10b). As shown before, the phase of det impedance is not altered by galvanic distortion (Figure 4.10b), but its magnitude is biased downward due to the shear and splitting parameters as with the det impedance from the distorted 1D data.

As with the 1D example, the main feature observed from the det and ssq impedances due to the effect of random galvanic distortion paramters is an irregular shift (Figure 4.11). The advantage of using the ssq impedances is evident

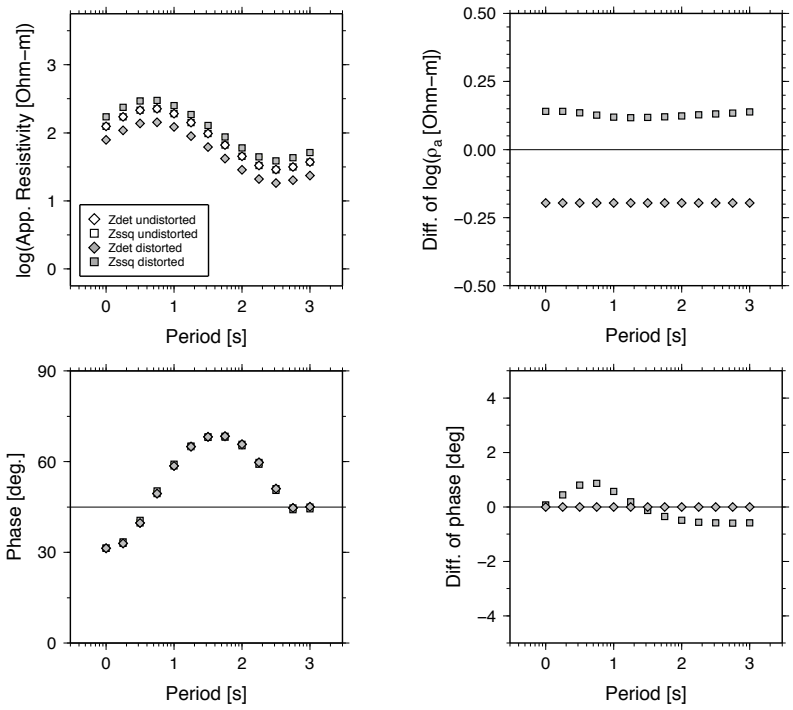

(a) (b)

Figure 4.10: (a) Corresponding det and ssq impedances of the undistorted and distorted impedances in Figure 4.9. (b) Difference between distorted and undistorted rotational invariant impedances.

when they are averaged (Figure 4.12). The error bar here is also the standard deviation. As with the 1D example, the average ssq impedances has a smaller error bar smaller than the average det impedances at the same strength of galvanic distortion. This supports the idea that the ssq impedance is less dispersed due to galvanic distortion. Also, the average det impedances is biased downward by the splitting and shear parameters.

To yield the models of the regional mean 1D conductivity profile, the average distorted det and ssq impedances are inverted with the same uncertainty and convergence condition as used in the 1D example. Without galvanic distortion, the average det and ssq impedances results in very similar models (Figure 4.13). The models estimated from the undistorted data both det and ssq impedances seem consistent with the theoretical models, which is obtanied by applying Eqs. (1.5) and (1.6) to the conductivity distribution within the area of interest (dashed frame in Figure 4.7). The discussion of the theoretical model is given in Section

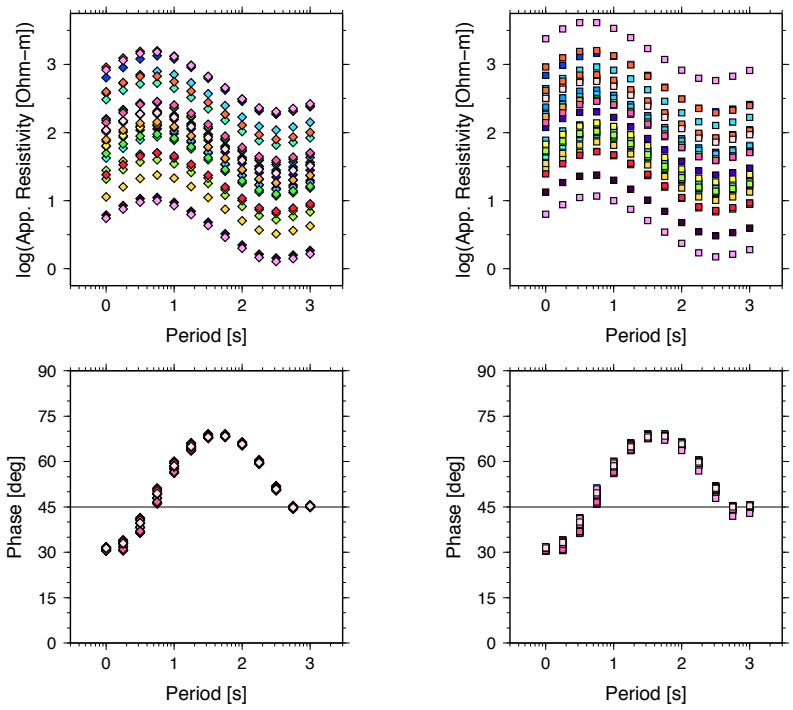

(a) (b)

Figure 4.11: (a) Det and (b) ssq impedances from the 3D example (as shown in Figures 4.8a and 4.8b, respectively) where a set of distortion parameters with an SD of 0.3 was applied.

4.3. As with the 1D example, when the galvanic distortion is included, the average det impedances will give the more conductive models of the regional mean 1D conductivity profile. On the contrary, using the average ssq impedances results in the models that are close to the model derived from the undistorted cases at any galvanic distortion strength. This result strongly supports the idea that the average ssq impedance is an promising parameter in estimating the model of the regional mean 1D conductivity profile.

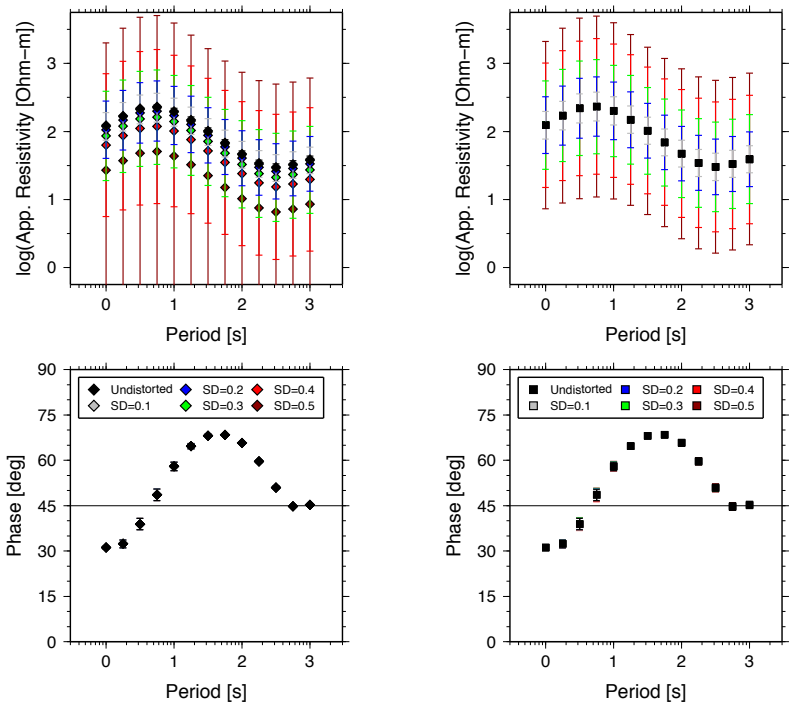

(a) (b)

Figure 4.12: Average (a) det and (b) ssq impedances from the 3D datasets distorted with different galvanic distortion strengths.

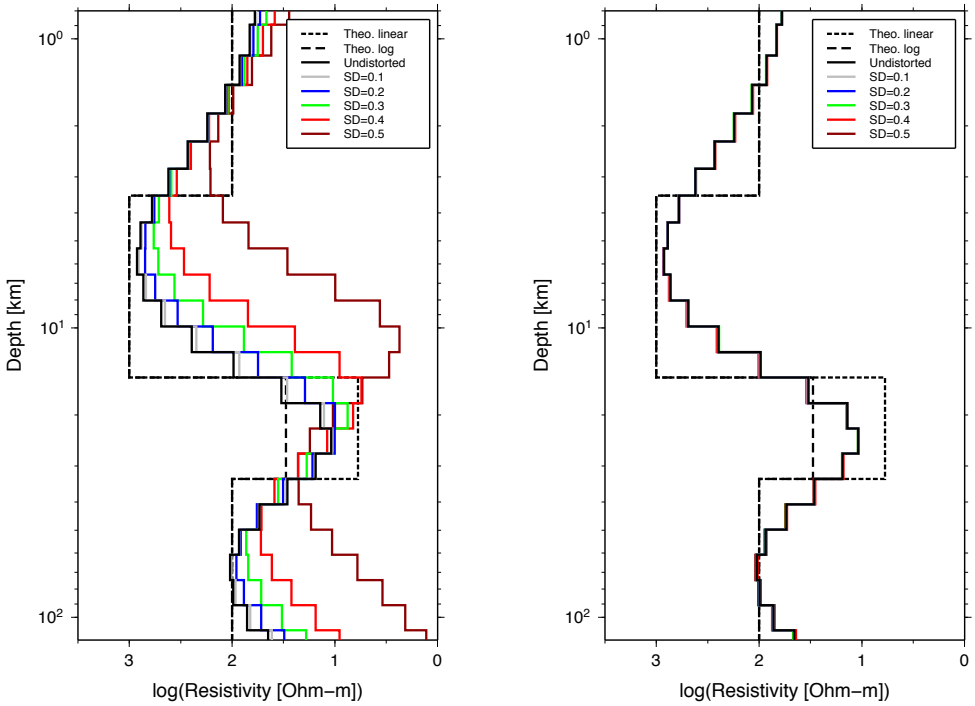

Figure 4.13: 1D models inverted from the average (a) det and (b) ssq impedances from the distorted 3D datasets (Figure 4.12). The theoretical model of the mean 1D profile from this setting is shown for comparison.

4.3 Consistency examination of the theoretical model of regional mean 1D conductivity profile

In analogy to the fact that the host layer Earth is absolutely unknown in reality, we proposed to compare the estimated model of the regional mean 1D conductivity profile with the theorectical model of the regional mean 1D conductivity profile instead of comparing it with the true layer Earth (e.g., the model in Figure 4.1a) in synthetic tests. In this section, we examined the consistency of the proposed theoretical model (Eqs. 1.5 and 1.6) and the estimated model of regional mean 1D conductivity profile with synthetic examples.

In conducting MT surveys and other geophysical methods, a number of observations are made to sufficiently cover the target structure with the typical site spacing to resolve the smallest scale target. This concept is analogous to the sampling theorem. To demonstrate the effect of the array size, in this consistency test, we test the array size that is larger than and comparable to the anomaly size at different locations.

We used the 3D models and the array setup (25 MT stations within an area of 80 km $\times$ 80 km) as used in Section 4.2. In this setup, the cluster is significantly larger than the anomaly. We put the cluster in the three different locations: central, northwest and northeast positions (Figure 4.14). At the center, the array is concentric with the anomaly, while at the northeast and northwest locations, the arrays are, respectively, dominated by the 300 and 3 Ω m anomalies. In this case, three clusters contain the same portion of conductive and resistive anomalies.

The estimated models of the regional mean 1D conductivity profiles from these clusters were calculated from the average ssq impedance. Note that only the ssq impedance is used in this section, because the galvanic distortion is not of concern. The theoretical models of the regional mean 1D conductivity profile were calculated using the given definitions from the conductivity in the clusters (e.g., dashed frames in Figure 4.14), and the MT responses from the theoretical models were then obtained using the analytic solution (Constable et al., 1987).

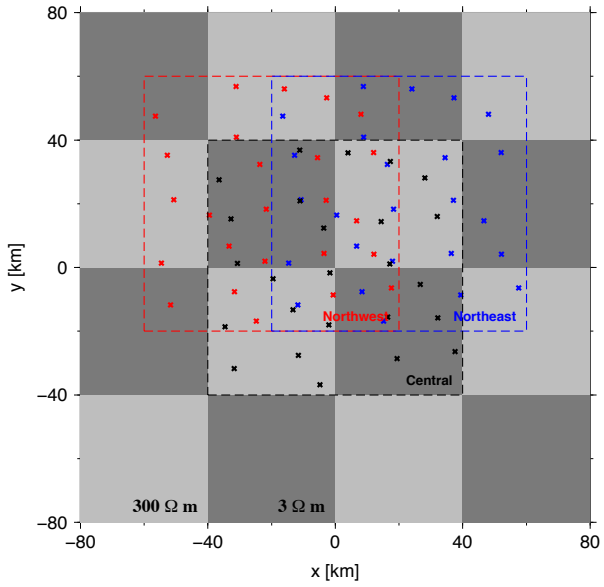

Figure 4.14: Checkerboard model with an anomaly size of 40 km × 40 km and resistivities of 3 (dark gray) and 300 (light gray) Ω m. The checkerboard anomaly was embedded in the lower crust layer. Three arrays of 25 MT stations (crosses) each with a size of 80 km × 80 km (dashed frames) were placed at the central (black), northeast (blue), and northwest (red) positions.

When the arrays are larger than the anomaly, the arrays contain the comparable portions of the resistive and conductive heterogeneities, even though they are at different locations. The estimated and theoretical models of the regional mean 1D conductivity profiles from different clusters are likely identical (Figure 4.15). In other words, the average approach is spatially independent for the large array. Hence, the average approach is a robust method to obtain the regional mean 1D conductivity profile. The smooth and step shapes of the estimated and theoretical models might be due to the smoothness constraint applied in the inversion.

Next, we demonstrate how array size affects the models of the regional mean 1D conductivity profile by decreasing the array size to 40 km × 40 km (Figure 4.16), which is equal to the anomaly size. The cluster locations were kept the same as in the previous test.

In this case, the theoretical models from different cluster locations are totally different (Figure 4.17a) because the clusters occupy different portions of resistive and conductive anomalies. The northwest cluster covers only the underlying

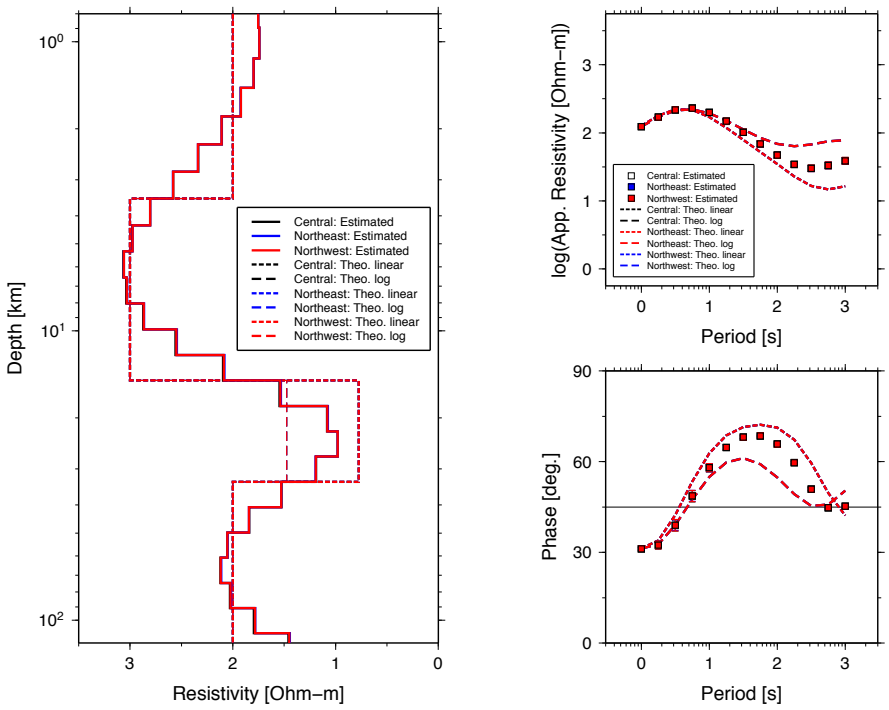

(a) (b)

Figure 4.15: (a) Theoretical (dashed lines) and estimated (solid lines) models of the mean 1D profiles obtained using the settings shown in Figure 4.14. (b) Corresponding MT responses from the theoretical (dashed line) and estimated (squares) models of the mean 1D profiles. The results obtained from different array locations are represented by lines and symbols of different colors.

3 Ω m anomaly, for example. Note that when the array resides on the layered-Earth like structure, e.g., the cluster on the northwest and northeast positions, the theoretical models from the log and the linear average definition are the same (Figure 4.17a). In constrast to the theoretical models, the estimated models of regional mean 1D profile remain spatially independent in this setup. This is because the inductive effect from the anomalies is indistinguishable from different array locations. It is expected that if the anomaly is significantly large or the cluster is very small, the estimation method would show the spatially dependent feature.

As expected, using the logarithmic average definition (Eq. 1.6) would give the less conductive structure (e.g., Figure 4.15a). Although, the theoretical models from the linear and log average definition are noticeably different (Figures 4.15a and 4.17a) when both conductive and resistive anomalied are contained in the array, they are both consistent with the estimated model. Hence, both defini-

tions are acceptable for calculating the theoretical model of the regional mean 1D conductivity profile.

When the array is significantly larger than the anomaly, the estimation and the theoretical definition are rather consistent. But, when the array is comparable or smaller than the anomaly, the inconsistency is clearly observed, particularly, at the depth where the anomalies are embedded (Figure 4.17). However, the inconsistency seems to be less evident when the cluster is located over the conductive anomaly (e.g., the northwest cluster), because of the nature of the electromagnetic induction that the conductive anomaly will produce significant inductive effect when compared to the resistive anomaly. This inconsistency is a consequence of an inappropriate design of the observation array, e.g., the cluster is not sufficiently large to cover the anomaly. The tests also suggest that the estimation of the regional mean 1D profile would be reliable with a large size of array.

In general, the exact dimension of the target structure is unknown. One may be able to approximate its from other information such as geological background or past studies. The observation array is then designed so as to cover the target structure. However, if the anomaly geometry is found to be comparable to the size of the array then the resulting conductivity image may be affected by the array location. One suggestion is to increase the array size by adding additional MT stations in order to get the reliable results.

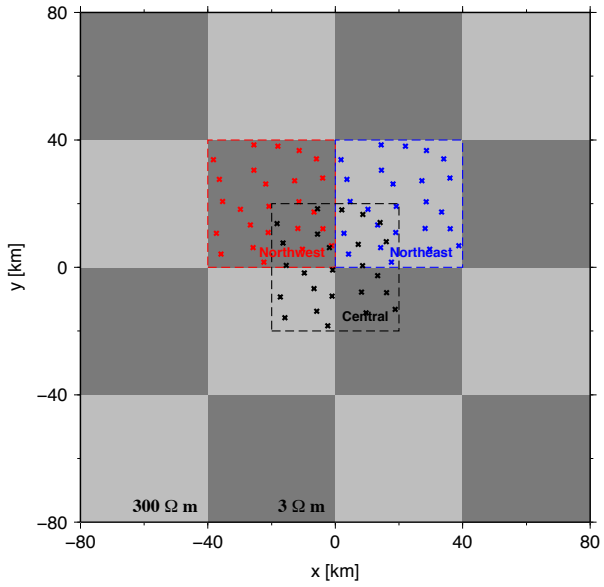

Figure 4.16: Same as Figure 4.15 for an array size of 40 km × 40 km.

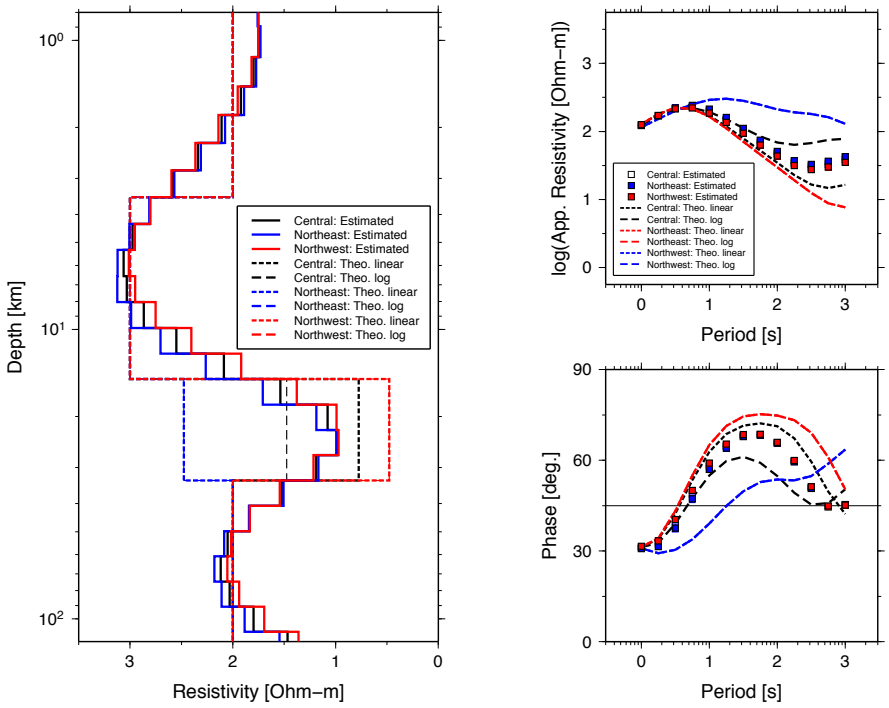

(a) (b)

Figure 4.17: Same as Figure 4.15 for the settings shown in Figure 4.16.

4.4 Local and regional distortion indicators

This section shows the example of local and regional distortion indicators (Eqs 3.19 and 3.24) derived from the synthetic 1D and 3D examples in Sections 4.1 and 4.2, respectively.

In this test, these local distortion indicators are obtained by applying Eq. (3.19) to the det and ssq impedances from the 1D dataset distorted with the distortion parameter with an SD of 0.3 (as shown in Figure 4.4), for example. As shown earlier, the local distortion indicators derived from distorted 1D data are shifted upward (greater than unity) and remain real-valued. The local distortion indicators are shifted irregularly depending on the strength of shear and splitting parameters at individual sites (Figure 4.18a). In addition, the calculated local distortion indicator from the data distorted with $(g, t, e, s) = (1.20, 0.11, -0.37, 0.49)$, for example, agrees well with the actual value (gray circles and dashed line in Figure 4.18a, respectively). Note that the actual local distortion indicator is calculated by substituting the shear and splitting parameters of -0.37 and 0.49 into Eq. (3.22).

For 3D cases, the local distortion indicators contain both the frequency dependent and independent features (Eq. 3.21). The frequency independent part is mainly due to the shear and splitting parameters, which are real-valued, while the frequency dependent part is ascribed by the difference between the ssq and det impedances at individual sites, which is complex-valued and rather weak in general. As with the 1D example, the example of local distortion indicators from distorted 3D data (Figure 4.21b) are also obtained by applying Eq. (3.19) to the 3D data distorted with the distortion parameter with an SD of 0.3 (as shown in Figure 4.11). In contrast to the 1D case, the local distortion indicators from distorted 3D data show a frequency-dependent feature and become complex-valued, which depends on how strong the inductive effect from the underlying structure is and the galvanic distortion strength posed in the data. The local distortion indicator derived from the data at the station `syn08`, which is distorted by (g, t, e, s) of $(1.20, 0.11, -0.37, 0.49)$, are compared with the actual value of the local distortion

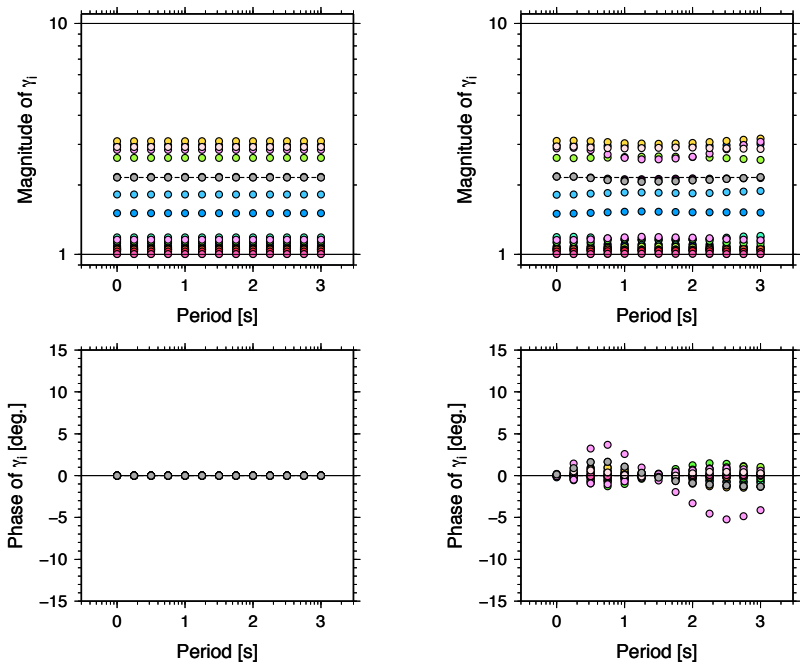

(a) (b)

Figure 4.18: Local distortion indicators from the distorted (a) 1D and (b) 3D data (in Sections 4.1 and 4.2, respectively) where a set of distortion parameters with an SD of 0.3 was applied. Examples of 1D and 3D data at station `syn08` distorted with $(g, t, e, s) = (1.20, 0.11, -0.37, 0.49)$ (gray circles) are compared with the actual values of the local distortion indicator at this station (dashed lines)

indicators. Although the local distortion indicator is deviated because of the inductive effect of the underlying structure, it still oscillates about the actual values (gray circles and dashed line in Figure 4.18b). Hence the local distortion indicator can be used to indicate the strength of shear and splitting effects.

However, if the strong 3D effect (e.g., coastal effect) or the inductive distortion is contained, the local distortion indicator would become very frequency dependent and rather complex valued. In such a case, the treatment of distortion as galvanic orgin is not allowed. In other words, the local distortion indicator is able to indicate the period range where the data is inductively distorted as well as galvanically distorted. Thus the local distortion indicator will help judge the validity of applying phase tensor, because the phase tensor is defined for the case with the galvanic distortion only.

The mean local distortion indicators $\bar{\gamma}_i$ of the 1D and 3D dataset dis-

torted with the set of distortion parameters with SD of 0.3 (Figures 4.19 and 4.20) are calculated using Eq. (3.23). Compared to the local distortion indicators (Figures 4.18a and 4.18b), it is more convenient to identify the site-to-site strength of the shear and splitting effect. They are shown in comparison with the actual local distortion indicators γ_i, which are calculated by substituting the synthetic shear and splitting parameters at each station into Eq. (3.19). We also define the percentage difference between the mean local distortion indicator and the actual local distortion indicators for validation purposes:

$$\mathcal{P}(\bar{\gamma}_i) = \frac{\bar{\gamma}_i - \gamma_i}{\gamma_i} \times 100\%. \tag{4.1}$$

In the 1D case, the mean local distortion indicator is able to correctly estimate the strength of galvanic distortion with zero difference (Figure 4.19). As shown earlier, the underlying structure may affect the local distortion indicator in 3D case as a frequency dependent contribution. Here, the error bar is set to the standard deviation in order to represent the dispersion of the frequency dependent part in the local distortion indicator. For example, the station `syn02` has the significant frequency-dependent variation. Although some errors in estimating the galvanic distortion strength appear in the distorted 3D data (Figure 4.20), they are still in the acceptable range.

The regional distortion indicator represents the effect of the shear and splitting parameters throughout the dataset. By averaging, the inductive effect from the underlying structure can be flattened out. The regional distortion indicator becomes real-valued, and its magnitude will indicate the strength of shear and splitting parameters on average. Here, we show the regional distortion indicators from 1D and 3D data distorted with different galvanic distortion strengths (Figure 4.21). They are derived from averaging the local distortion indicators using Eq. (3.24). As with the average det and ssq impedances shown in Figure 4.12, the error bar is the SD of local distortion indicators, i.e., it represents the dispersion of the local distortion indicators in each dataset. The stronger galvanic distortion tends to show the larger error bar in this case. As with the local distortion indicator,

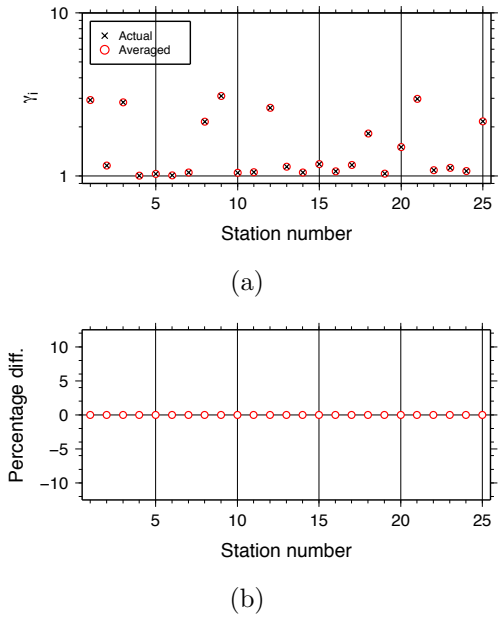

Figure 4.19: (a) Comparison of actual local distortion indicators (crosses) with the mean local distortion indicators (red circles) from the 1D example, where a set of distortion parameters with an SD of 0.3 was applied (Figure 4.4). (b) Percentage difference between the mean local distortion indicators and the actual ones.

the indicators from 1D data is definitely real-valued, and its magnitude is consistent with the galvanic distortion strength. As expected, the regional distortion indicators from distorted 3D datasets are rather real-valued, and its magnitude is comparable to the regional distortion indicators from distorted 1D datasets at the same galvanic distortion strength. In conclusion, the regional distortion indicator can estimate the strength of galvanic distortion – shear and splitting parameters – contained in MT datasets fairly well.

From the synthetic examples, the local distortion indicator is able to determine the existence and strength of galvanic distortion, if contained in the data. One of its possible and practical uses is to omit or decrease the constraints on the data from the stations that are heavily distorted (e.g., `syn01` and `syn02` in the example dataset), if the number of such stations is low. When the number of heavily distorted stations is significant, the regional distortion indicator will be noticeable. The distortion removal or proper treatments, for example, the inversion simultaneously with galvanic distortion (e.g., Sasaki and Meju, 2006;

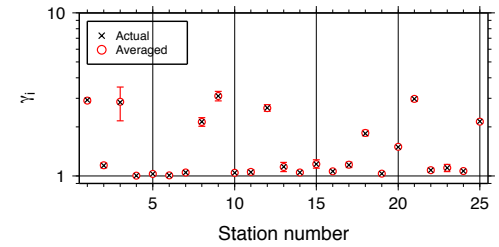

(a)

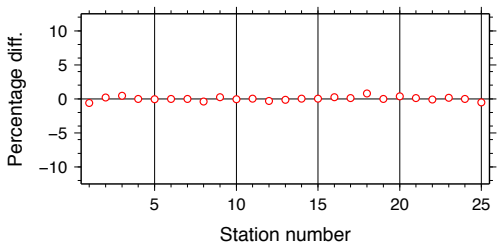

(b)

Figure 4.20: Same as Figure 4.19 for the 3D example

Avdeeva et al., 2015), may be necessary. However, if the magnitude of regional distortion indicator is rather small, i.e., the whole dataset is weakly distorted, such a complicated computation may be avoided.

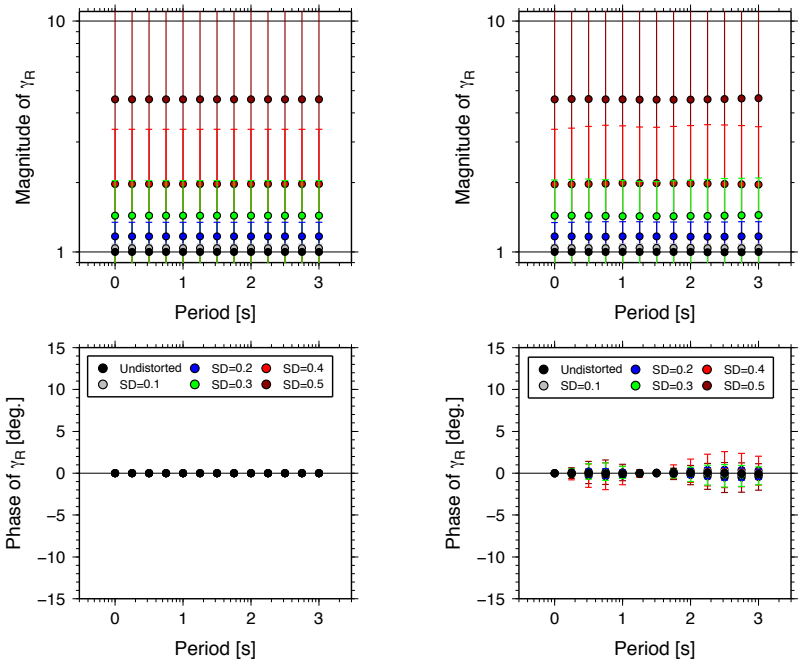

Figure 4.21: Regional distortion indicators from (a) 1D and (b) 3D examples with different galvanic distortion strengths.

4.5 Apparent gains

This section shows the example of apparent det and ssq gains (Eqs. 3.26 and 3.27) derived from the synthetic 1D and 3D examples in Sections 4.1 and 4.2, respectively, and we also verify estimating site gain in the data by using the mean apparent gains (Eqs 3.32 and 3.33).

First, we show the examples of the apparent gains from the 1D data and 3D data at the station `syn08`. These data are distorted with the distortion parameters (g, t, e, s) is $(1.20, 0.11, -0.37, 0.49)$ (Figure 4.22). As proven, the apparent gains from 1D data are real-valued and frequency independent. The apparent ssq gain accurately estimates the synthetic site gain, while the apparent det gain, here, is biased downward because of shear and splitting parameters (Figure 4.22a). In the 3D case, the apparent gains show frequency dependent features and become weakly complex-valued number due to the inductive effect of the underlying 3D

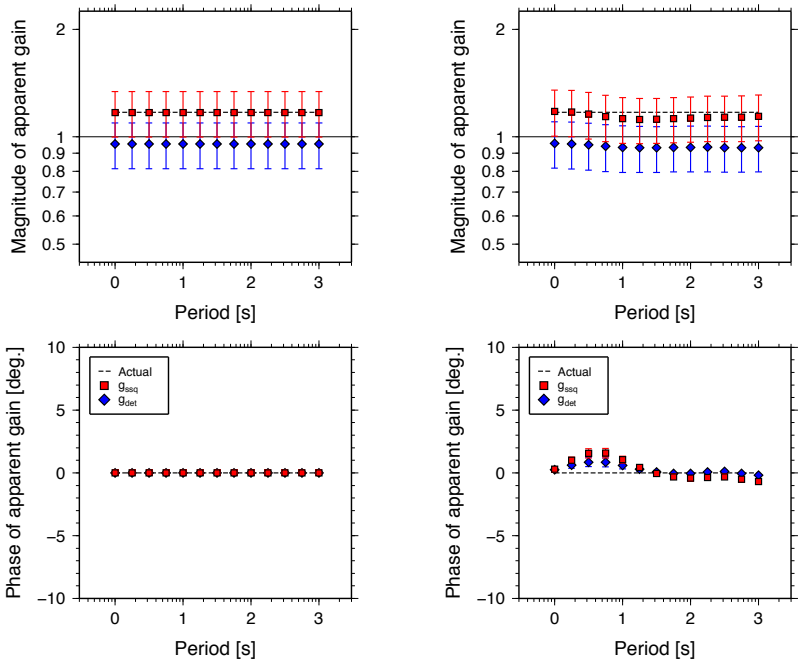

Figure 4.22: Det (diamonds) and ssq (squares) apparent gains from (a) the 1D data and (b) station `syn08` in the 3D data. The distortion parameters with an SD of 0.3 are applied to both 1D and 3D datasets. A synthetic site gain (dashed line) of 1.20 was applied at this station.

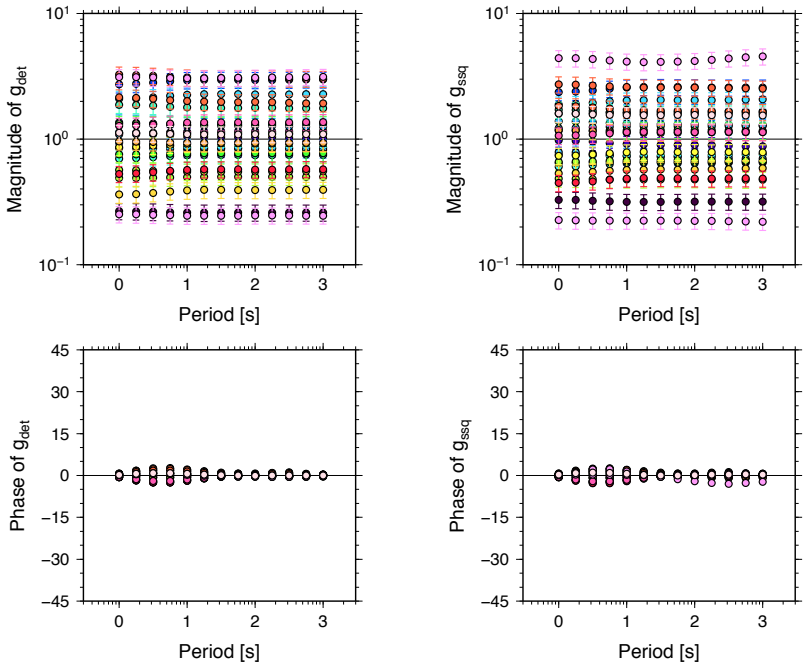

Figure 4.23: The apparent (a) det and (b) ssq gains derived from the 3D example, where a set of distortion parameters with an SD of 0.3 was applied.

heterogeneity (Figure 4.22b). However, the apparent ssq gain still agrees with the synthetic site gain within the uncertainty. As with the 1D example, the apparent det gain is biased downward by the distortion parameters. Note that the error bars (in Figure 4.22) are derived from the standard error obtained from averaging the det and ssq impedances (Figure 4.12). Therefore, if the distortion is very intense, the apparent gains will be less constrained.

The apparent det and ssq gains as a function of period from the 3D datasets distorted with the distortion parameters with an SD of 0.3 are shown in Figure 4.23. The apparent gains have a combination of the frequency dependence and independence. The frequency-independent feature is upto the site gain contained at each station, while the frequency-dependent feature strongly depends on how strong the inductive effect of the underlying 3D structure is.

However, to yield the more meaningful interpretation of them, we calculate the mean apparent ssq and det gains using Eqs (3.32) and (3.33). To validate the mean apparent gains, we also define the percentage difference between the

mean apparent gains (Eqs 3.32 and 3.33) and the synthetic site gain g_i:

$$\mathcal{P}(\bar{g}_i^{\text{ssq}}) = \frac{\bar{g}_i^{\text{ssq}} - g_i}{g_i} \times 100\% \tag{4.2}$$

$$\mathcal{P}(\bar{g}_i^{\text{det}}) = \frac{\bar{g}_i^{\text{det}} - g_i}{g_i} \times 100\%. \tag{4.3}$$

From the 1D dataset, the mean apparent ssq gain correctly estimates the synthetic site gain in the data as confirmed by the zero percentage difference (Figure 4.24). Conversely, the mean apparent det gain would be either the overestimate or the underestimate of the site gain depending on the galvanic distortion strength, which could be pointed out by the local distortion indicator at individual sites (Figures 4.19 and 4.20). This is because the det impedance is affected by the shear and splitting parameters. If the distortion at sites is stronger than average, the mean apparent det gain will be an underestimate (e.g., `syn01`, `syn03`, `syn09`). On the contrary, if the distortion at sites is weaker than average, the mean apparent det gain will be an overestimate (e.g., `syn04`, `syn05`). Note that error bars in this figure are derived from the error propagation rule when calculating Eqs. (3.32) and (3.33). Although the mean apparent det gain agrees with the actual value within the uncertainty range, the mean apparent ssq gain is sitll the favorable choice.

As shown before, the inductive effect from 3D structure can cause the frequency-dependent variation in the apparent gains (Figure 4.24). It may result in some error in estimating the site gain with the mean apparent gain. For instance, the mean apparent ssq gains from the stations over the conductive structure (e.g., `syn07`, `syn19`) underestimate the synthetic site gains, i.e., less than the actual value (Figure 4.25), as seen from the negative percentage difference. On the contrary, if the stations are located over the resistive structure (e.g., `syn04`, `syn09`), the mean apparent gain is overestimated. Despite of this, the estimate of site gain from the mean apparent ssq gain still agrees with the synthetic values within the statistical uncertainty.

It is believed that the site gain is undeterminable without other inde-

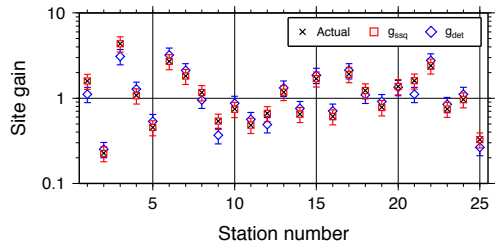

(a)

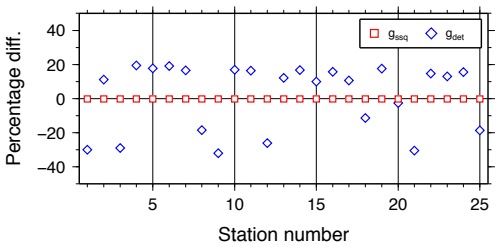

(b)

Figure 4.24: (a) Comparison of actual site gains (crosses) with the mean apparent det (diamonds) and ssq (squares) gains from the 1D example, where a set of distortion parameters with an SD of 0.3 was applied. (b) Percentage difference between the mean apparent gains and the actual site gains

pendent geophysical data (e.g., Groom et al., 1993; Bibby et al., 2005). From the theoretical derivation and the synthetic examples, the apparent ssq gain is shown to be the promising parameter for the site gain estimation. It is also important to note that this information can be gleaned from MT data alone. This parameter would help correcting the magnitude of MT impedances.

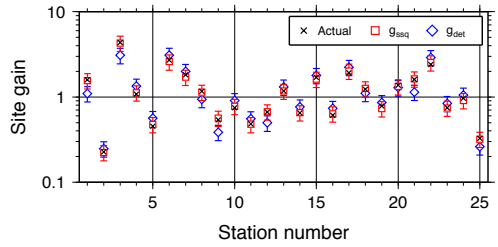

(a)

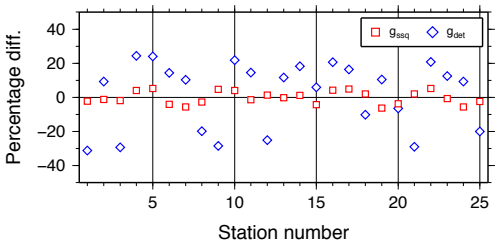

(b)

Figure 4.25: Same as Figure 4.24 for the 3D example

CHAPTER V

CONCLUSIONS

One strategy in performing 3D inversion is to start by searching for a reliable model of the regional mean 1D conductivity profile which is able to minimize the variance of the conductivity contrast. Traditionally, the model of the regional mean 1D conductivity profile was estimated from the Berdichevsky average, i.e., the average det impedance, which is able to smooth out the galvanic effect from small-scale local structure. However, it had been introduced before the knowledge of galvanic distortion was well established. Therefore, the effect of the galvanic distortion on the Berdichevsky average has never been examined.

Galvanic distortion is the spatial aliasing in MT data by small-scale near-surface heterogeneity, and it is unavoidable in general. The question is how reliable is the model obtained from the Berdichevsky average with the presence of galvanic distortion. The ssq impedance is therefore introduced as another rotation invariant candidate to challenge this problem. The det and ssq impedances derived from the distorted MT impedance are algebraically examined using the Groom–Bailey model of galvanic distortion. It is found that the det impedance is biased downward by the shear and splitting parameters, while the ssq impedance is less sensitive to these distortion parameters. This major finding urges us to redefine the Berdichevsky average with the ssq impedance in order to reliably estimate the model of the regional mean 1D conductivity profile. From the synthetic examples, the models obtained from the traditional Berdichevsky average may overestimate the regional mean 1D conductivity profile. Regardless of the galvanic distortion strength, the average ssq impedance is theoretically and numerically proven to be the promising method to accurately estimate the model of the regional mean 1D conductivity profile.

The definitions for the theoretical model of the regional mean 1D conductivity profile are also introduced. Instead of comparing the estimated model with the host background, which is not viable in reality, we are able to compare the estimated model with the theoretical model from the given definitions. The theoretical model could be calculated using either a linear or logarithmic scale average depending on the choice of model parameters in optimization. The numerical results show that the theoretical models are consistent with the estimated model when the MT array is larger than the anomaly size. Therefore, the theoretical and estimated model of the regional mean 1D conductivity profile is reliable with the appropriate size of MT array.

In addition, the concept of galvanic distortion-related parameters was first introduced. Using these parameters enables us to indicate the existence of galvanic distortion and also to quantify its strength. Two type of indicators are defined from the det and ssq impedances, the local and regional distortion indicators and the apparent gains. Their functions are totally different. The former is to indicate the strength of the shear and splitting effect, and the latter is to be a good approximate of site gain, which is generally claimed to be the undeterminable distortion parameter. Note that the effect of twist cannot be ascertained because both det and ssq impedance are rotationally invariant. One possible and practical use of the local distortion indicator is to point out heavily distorted MT data, which may be rejected in interpretation. The regional distortion indicator can be used to determine the necessity of the proper treatment or removal of galvanic distortion, which may be algebraically complicated and computationally expensive.

The ultimate goal of this thesis is to handle the problem of galvanic distortion, particularly in imaging 3D conductivity structure. In conclusion, we propose to estimate the model of the regional mean 1D conductivity profile, less biased by the galvanic distortion, with the average ssq impedance and make the distortion strength quantifiable with the galvanic distortion indicators. The theoretical derivation of them was verified by a series of synthetic examples. With the proposed method, the unbiased models of the regional mean 1D conductivity profile could be obtained even if the datasets are distorted. The galvanic distor-

tion indicators would help determine the need of applying the augmented approach, e.g., 3D inversion including galvanic distortion, or the omission of heavily distorted data. The proposed method to reliably estimate the model of the regional mean 1D conductivity profile from the set of distorted MT data and the concept of galvanic distortion indicators would be essential and instructive in 3D inversion.

REFERENCES

Amatyakul, P., Rung-Arunwan, T., and Siripunvaraporn, W. (2015). A pilot magnetotelluric survey for geothermal exploration in Mae Chan region, northern Thailand. *Geothermics*, 55(0):31 – 38.

Arango, C., Marcuello, A., Ledo, J., and Queralt, P. (2009). 3D magnetotelluric characterization of the geothermal anomaly in the Llucmajor aquifer system (Majorca, Spain). *Journal of Applied Geophysics*, 68(4):479 – 488.

Avdeev, D. (2005). Three-dimensional electromagnetic modelling and inversion from theory to application. *Surveys in Geophysics*, 26(6):767–799.

Avdeev, D. and Avdeeva, A. (2009). 3D magnetotelluric inversion using a limited-memory quasi-Newton optimization. *Geophysics*, 74(3):F45–F57.

Avdeeva, A., Moorkamp, M., Avdeev, D., Jegen, M., and Miensopust, M. (2015). Three-dimensional inversion of magnetotelluric impedance tensor data and full distortion matrix. *Geophysical Journal International*, 202(1):464–481.

Baba, K., Utada, H., Goto, T. N., Kasaya, T., Shimizu, H., and Tada, N. (2010). Electrical conductivity imaging of the Philippine Sea upper mantle using seafloor magnetotelluric data. *Physics of the Earth and Planetary Interiors*, 183(1–2):44 – 62. Special Issue on Deep Slab and Mantle Dynamics.

Bahr, K. (1988). Interpretation of the magnetotelluric impedance tensor: Regional induction and local telluric distortion. *Journal of Geophysics*, 62:119–127.

Banks, R. J. (1969). Geomagnetic variations and the electrical conducivity of the upper mantle. *Geophysical Journal - Royal Astronomical Society*, 17:457–487.

Berdichevsky, M., Vanyan, L., Kuznetsov, V., Levadny, V., Mandelbaum, M., Nechaeva, G., Okulessky, B., Shilovsky, P., and Shpak, I. (1980). Geoelectrical model of the Baikal region. *Physics of the Earth and Planetary Interiors*, 22(1):1–11.

Bibby, H. M., Caldwell, T. G., and Brown, C. (2005). Determinable and non-determinable parameters of galvanic distortion in magnetotellurics. *Geophysical Journal International*, 163:915–930.

Booker, J. R. (2014). The magnetotelluric phase tensor: A critical review. *Surveys in Geophysics*, 35(1):7–40.

Boonchaisuk, S., Siripunvaraporn, W., and Ogawa, Y. (2013). Evidence for middle Triassic to Miocene dual subduction zones beneath the Shan–Thai terrane, western Thailand from magnetotelluric data. *Gondwana Research*, 23(4):1607 – 1616.

Cagniard, L. (1953). Basic theory of the magneto-telluric method of geophysical prospecting. *Geophysics*, 18(3):605–635.

Caldwell, T. G., Bibby, H. M., and Brown, C. (2004). The magnetotelluric phase tensor. *Geophysical Journal International*, 158:457–469.

Chapman, S. and Price, A. (1930). The electric and magnetic state of the interior of the earth, as inferred from terrestrial magnetic variations. *Philosophical Transactions of the Royal Society of London. Series A, Containing Papers of a Mathematical or Physical Character*, pages 427–460.

Chave, A. D. and Jones, A. G. (2012). *The Magnetotelluric Method Theory and Practice*. Cambridge University Press, 1st edition.

Chave, A. D. and Smith, J. T. (1994). On the electric and magnetic galvanic distortion tensor decompositions. *Journal of Geophysical Research*, 99(B3):4669–4682.

Chave, A. D. and Thomson, D. (2004). Bounded influence magnetotelluric response function estimation. *Geophysical Journal International*, 157:988–1006.

Constable, S. C., Parker, R. L., and Constable, C. G. (1987). Occam's inversion: A practical algorithm for generating smooth models from electromagnetic sounding data. *Geophysics*, 52(3):289–300.

DeGroot-Hedlin, C. (1991). Removal of static shift in two dimensions by regularized inversion. *Geophysics*, 56(12):2102.

Egbert, G. D. (1997). Robust multiple-station magnetotelluric data processing. *Geophysical Journal International*, 130(2):475–496.

Fukao, Y., Koyama, T., Obayashi, M., and Utada, H. (2004). Trans-Pacific temperature field in the mantle transition region derived from seismic and electromagnetic tomography. *Earth and Planetary Science Letters*, 217(3):425–434.

Gómez-Treviño, E., Hernández, F. J. E., and Jones, J. M. R. (2013). Effect of galvanic distortions on the series and parallel magnetotelluric impedances and comparison with other responses. *Geofísica Internacional*, 52(2):135–152.

Gómez-Treviño, E., Hernández, F. J. E., and Jones, J. M. R. (2014). Quadratic solution for the 2-D magnetotelluric impedance tensor distorted by 3-D electro-galvanic effects. *Geophysical Journal International*, 198(3):1795–1804.

Groom, R. and Bahr, K. (1992). Corrections for near surface effects: Decomposition of the magnetotelluric impedance tensor and scaling corrections for regional resistivities: A tutorial. *Surveys in Geophysics*, 13(4-5):341–379.

Groom, R. W. and Bailey, R. C. (1989). Decomposition of magnetotelluric impedance tensors in the presence of local three-dimensional galvanic distortion. *Journal of Geophysical Research: Solid Earth*, 94(B2):1913–1925.

Groom, R. W., Kurtz, R. D., Jones, A. G., and Boerner, D. E. (1993). A quantitative methodology to extract regional magnetotelluric impedances and determine the dimension of the conductivity structure. *Geophysical Journal International*, 115:1095–1118.

Heise, W., Bibby, H. M., Caldwell, T. G., Bannister, S. C., Ogawa, Y., Takakura, S., and Uchida, T. (2007). Melt distribution beneath a young continental rift: The Taupo Volcanic Zone, New Zealand. *Geophysical Research Letters*, 34(14). L14313.

Heise, W., Caldwell, T. G., Bibby, H. M., and Bannister, S. C. (2008). Three-dimensional modelling of magnetotelluric data from the Rotokawa geothermal field, Taupo Volcanic Zone, New Zealand. *Geophysical Journal International*, 173(2):740–750.

Hohmann, G. W. (1975). Three-dimensional induced polarization and electromagnetic modeling. *Geophysics*, 40(2):309–324.

Jiracek, G. R. (1990). Near-surface and topographic distortions in electromagnetic induction. *Surveys in Geophysics*, 11(2-3):163–203.

Jones, A. G. (1999). Imaging the continental upper mantle using electromagnetic methods. *Lithos*, 48:57–80.

Jones, A. G. (2011). Three-dimensional galvanic distortion of three-dimensional regional conductivity structures: Comment on "Three-dimensional joint inversion for magnetotelluric resistivity and static shift distributions in complex media" by Yutaka Sasaki and Max A. Meju. *Journal of Geophysical Research: Solid Earth (1978–2012)*, 116(B12).

Karato, S. (1990). The role of hydrogen in the electrical conductivity of the upper mantle. *Nature*, 347:272–273.

Kelbert, A., Egbert, G. D., and Schultz, A. (2008). Non-linear conjugate gradient inversion for global em induction: resolution studies. *Geophysical Journal International*, 173(2):365–381.

Kelbert, A., Meqbel, N., Egbert, G. D., and Tandon, K. (2014). ModEM: A modular system for inversion of electromagnetic geophysical data. *Computers & Geosciences*, 66(0):40 – 53.

Kelbert, A., Schultz, A., and Egbert, G. (2009). Global electromagnetic induction constraints on transition-zone water content variations. *Nature*, 460:1003–1007.

Koyama, T., Shimizu, H., Utada, H., Ichiki, M., Ohtani, E., and Hae, R. (2006). Water content in the mantle transition zone beneath the North Pacific derived from the electrical conductivity anomaly. *Geophysical Monograph Series*, 168:171.

Kuvshinov, A. and Semenov, A. (2012). Global 3-D imaging of mantle electrical conductivity based on inversion of observatory C-responses—I. An approach and its verification. *Geophysical Journal International*, 189(3):1335–1352.

Kuvshinov, A. V. (2008). 3-D global induction in the oceans and solid earth: Recent progress in modeling magnetic and electric fields from sources of magnetospheric, ionospheric and oceanic origin. *Surveys in Geophysics*, 29(2):139–186.

Kuvshinov, A. V. (2011). Deep electromagnetic studies from land, sea, and space: Progress status in the past 10 years. *Surveys in Geophysics*.

Ledo, J. (2005). 2-D versus 3-D magnetotelluric data interpretation. *Surveys in Geophysics*, 26(5):511–543.

Lezaeta, P. and Haak, V. (2003). Beyond magnetotelluric decomposition: Induction, current channeling, and magnetotelluric phases over 90. *Journal of Geophysical Research: Solid Earth (1978–2012)*, 108(B6).

McNeice, G. and Jones, A. (2001). Multisite, multifrequency tensor decomposition of magnetotelluric data. *Geophysics*, 66(1):158–173.

Muñoz, G. (2013). Exploring for geothermal resources with electromagnetic methods. *Surveys in Geophysics*, pages 1–22.

Muller, M., Jones, A., Evans, R., Grütter, H., Hatton, C., Garcia, X., Hamilton, M., Miensopust, M., Cole, P., Ngwisanyi, T., Hutchins, D., Fourie, C., Jelsma, H., Evans, S., Aravanis, T., Pettit, W., Webb, S., and Wasborg, J. (2009). Lithospheric structure, evolution and diamond prospectivity of the Rehoboth Terrane and western Kaapvaal Craton, southern Africa: Constraints from broadband magnetotellurics. *Lithos*, 112, Supplement 1:93 – 105. Proceedings of the 9th International Kimberlite Conference9th International Kimberlite Conference.

Ogawa, Y., Jones, A. G., Unsworth, M. J., Booker, J. R., Lu, X. Y., Crave, J., Roberts, B., Parmelee, J., and Faquharson, C. (1996). Deep electrical conductivity structures of the Appalachian Orogen in the southeastern U.S. *Geophysical Research Letters*, 23(13):1597–1600.

Oldenburg, D. and Ellis, R. (1993). Efficient inversion of magnetotelluric data in two dimensions. *Physics of the Earth and Planetary Interiors*, 81(1–4):177 – 200.

Patro, P. K., Uyeshima, M., and Siripunvaraporn, W. (2013). Three-dimensional inversion of magnetotelluric phase tensor data. *Geophysical Journal International*, 192(1):58–66.

Pedersen, L. B. and Engels, M. (2005). Routine 2D inversion of magnetotelluric data using the determinant of the impedance tensor. *Geophysics*, 70(2):G33–G41.

Pellerin, L., Johnston, J. M., and Hohmann, G. W. (1996). A numerical evaluation of electromagnetic methods in geothermal exploration. *Geophysics*, 61(1):121–130.

Rikitake, T. (1946). Notes on the electromagnetic induction within the earth. *Bulletin Earthquake Research Institute*, 24:1–9.

Romo, J. M., Gómez-Treviño, E., and Esparza, F. J. (2005). Series and parallel transformations of the magnetotelluric impedance tensor: theory and applications. *Physics of the Earth and Planetary Interiors*, 150:63–83.

Rung-Arunwan, T., Siripunvaraporn, W., and Utada, H. (2016). On the Berdichevsky average. *Physics of the Earth and Planetary Interiors*. In Press.

Sasaki, Y. (2001). Full 3-D inversion of electromagnetic data on PC. *Journal of Applied Geophysics*, 46(1):45–54.

Sasaki, Y. and Meju, M. A. (2006). Three-dimensional joint inversion for magnetotelluric resistivity and static shift distributions in complex media. *Journal of Geophysical Research: Solid Earth (1978–2012)*, 111(B5).

Seama, N., Baba, K., Utada, H., Toh, H., Tada, N., Ichiki, M., and Matsuno, T. (2007). 1-D electrical conductivity structure beneath the Philippine Sea: Results from an ocean bottom magnetotelluric survey. *Physics of the Earth and Planetary Interiors*, 162(1-2):2–12.

Semenov, A. and Kuvshinov, A. (2012). Global 3-D imaging of mantle conductivity based on inversion of observatory C-responses—II. Data analysis and results. *Geophysical Journal International*, 191(3):965–992.

Shimizu, H., Koyama, T., Baba, K., and Utada, H. (2010). Revised 1-D mantle electrical conductivity structure beneath the north Pacific. *Geophysical Journal International*, 180:1030–1048.

Siripunvaraporn, W. and Egbert, G. (2009). WSINV3DMT: Vertical magnetic field transfer function inversion and parallel implementation. *Physics of the Earth and Planetary Interiors*, 173(3-4):317–329.

Siripunvaraporn, W., Egbert, G., Lenbury, Y., and Uyeshima, M. (2005). Three-dimensional magnetotelluric inversion: Data-space method. *Physics of the Earth and Planetary Interiors*, 150(1-3 SPEC. ISS.):3–14.

Smirnov, M. Y. and Egbert, G. (2012). Robust principal component analysis of electromagnetic arrays with missing data. *Geophysical Journal International*, 190(3):1423–1438.

Smith, J. T. (1995). Understanding telluric distortion matrices. *Geophysical Journal International*, 122:219–226.

Spitz, S. (1985). The magnetotelluric impedance tensor properties with respect to rotations. *Geophysics*, 50(10):1610–1617.

Swift, C. (1967). *A magnetotelluric investigation of an electrical conductivity anomaly in the south-western United States*. PhD thesis, Massachusetts Institute of Technology, Cambridge, MA, U.S.A.

Szarka, L., Ádám, A., and Menvielle, M. (2005). A field test of imaging properties of rotational invariants of the magnetotelluric impedance tensor. *Geophysical Prospecting*, 53:325–334.

Szarka, L. and Menvielle, M. (1997). Analysis of rotational invariants of the magnetotelluric impedance tensor. *Geophysical Journal International*, 129(1):133–142.

Szarka, L., Menvielle, M., and Spichak, V. (2000). Imaging properties of apparent resistivities based on rotational invariants of the magnetotelluric impedance tensor. *Acta Geodaetica et Geophysica Hungarica*, 35(2):149–175.

Tada, N., Baba, K., and Utada, H. (2014). Three-dimensional inversion of seafloor magnetotelluric data collected in the Philippine Sea and the western margin of the northwest Pacific Ocean. *Geochemistry, Geophysics, Geosystems*.

Tarits, P. (1994). Electromagnetic studies of global geodynamic processes. *Surveys in Geophysics*, 15(2):209–238.

Tietze, K., Ritter, O., and Egbert, G. D. (2015). 3-D joint inversion of the magnetotelluric phase tensor and vertical magnetic transfer functions. *Geophysical Journal International*, 203(2):1128–1148.

Tikhonov, A. (1950). On determining electrical characteristics of the deep layers of the earth's crust. *Doklady*, 73(2):295–297.

Tournerie, B. and Chouteau, M. (2002). Analysis of magnetotelluric data along the Lithoprobe seismic line 21 in the Blake River Group, Abitibi, Canada. *Earth, planets and space*, 54(5):575–589.

Tuncer, V., Unsworth, M. J., Siripunvaraporn, W., and Craven, J. A. (2006). Audio-magnetotelluric exploration for unconformity uranium deposits in the Athabasca Basin, Saskatachewan, Canada. *SEG Technical Program Expanded Abstracts*, 25(1):1328–1332.

Türkoğlu, E., Unsworth, M., and Pana, D. (2009). Deep electrical structure of northern Alberta (Canada): Implications for diamond exploration. *Canadian Journal of Earth Sciences*, 46(2):139–154.

Uchida, T. and Sasaki, Y. (2006). Stable 3D inversion of MT data and its application to geothermal exploration. *Exploration Geophysics*, 37(3):223–230.

Unsworth, M. (2010). Magnetotelluric studies of active continent-continent collisions. *Surveys in Geophysics*, 31(2):137–161.

Unsworth, M., Soyer, W., Tuncer, V., Wagner, A., and Barnes, D. (2007). Hydrogeologic assessment of the Amchitka Island nuclear test site (Alaska) with magnetotellurics. *Geophysics*, 72(3):B47–B57.

Utada, H., Koyama, T., Obayashi, M., and Fukao, Y. (2009). A joint interpretation of electromagnetic and seismic tomography models suggests the mantle transition zone below Europe is dry. *Earth and Planetary Science Letters*, 281(3):249–257.

Utada, H. and Munekane, H. (2000). On galvanic distortion of regional three-dimensional magnetotelluric impedances. *Geophysical Journal International*, 140:385–398.

Wang, D. J., Mookherjee, M., Xu, Y. S., and Karato, S. I. (2006). The effect of water on the electrical conductivity of olivine. *Nature*, 443:977–980.

Weaver, J. T., Agarwal, A. K., and Lilley, F. E. M. (2000). Characterization of the magnetotelluric tensor in terms of its invariants. *Geophysical Journal International*, 141(2):321–336.

Yang, J., Min, D.-J., and Yoo, H.-S. (2010). Sea effect correction in magnetotelluric (MT) data and its application to MT soundings carried out in Jeju Island, Korea. *Geophysical Journal International*, 182(2):727–740.

Yoshino, T., Matsuzaki, T., Yamashita, S., and Katsura, T. (2006). Hydrous olivine unable to account for conductivity anomaly at the top of the asthenosphere. *Nature*, 443:973–976.

BIOGRAPHY

NAME	Mr. Tawat Rung-Arunwan
DATE OF BIRTH	2nd November 1985
PLACE OF BIRTH	Chonburi, Thailand
INSTITUTIONS ATTENDED	Mahidol University, 2004–2007 Bachelor of Science (Physics) Mahidol University, 2004–2010 Master of Science (Physics) Mahidol University, 2010–2016 Doctor of Philosophy (Physics)
SCHOLARSHIPS	Thailand Center of Excellence in Physics, Commission of Higher Education, Ministry of Education, Thailand The internship program, the Earthquake Research Institute, the University of Tokyo, Japan
E-MAIL	t.rungarunwan@gmail.com